Allosteric inhibition of a stem cell RNA-binding protein by an intermediary metabolite

Carina C. Clingman, Laura M. Deveau, Samantha A. Hay, Ryan M. Genga, Shivender M.D. Shandilya, Francesca Massi, Sean P. Ryder*

Department of Biochemistry and Molecular Pharmacology, University of Massachusetts Medical School, Worcester, MA, 01605, USA

The authors declare they have no competing interests concerning this manuscript.

*Corresponding Author: Sean.Ryder@umassmed.edu

Phone: 508-856-1372

Fax: 508-856-6464

Address: 364 Plantation Street; LRB-906; Worcester, MA, 01605; USA

Abstract

Gene expression and metabolism are coupled at numerous levels. Cells must sense and respond to nutrients in their environment, and specialized cells must synthesize metabolic products required for their function. Pluripotent stem cells have the ability to differentiate into a wide variety of specialized cells. How metabolic state contributes to stem cell differentiation is not understood. Here, we show that RNA-binding by the stem cell translation regulator Musashi-1 (MSI1) is allosterically inhibited by 18-22 carbon ω-9 monounsaturated fatty acids. The fatty acid binds to the N-terminal RNA Recognition Motif (RRM) and induces a conformational change that prevents RNA association. Musashi proteins are critical for development of the brain, blood, and epithelium. We identify stearoyl-CoA desaturase-1 as a MSI1 target, revealing a feedback loop between ω-9 fatty acid biosynthesis and MSI1 activity. We propose that other RRM proteins could act as metabolite sensors to couple gene expression changes to physiological state.

Introduction

The RNA-binding protein Musashi-1 (MSI1) is expressed in stem and progenitor cells of neural and epithelial lineage. In the central nervous system, MSI1 is expressed in astrocytes and committed glial and neural progenitor cells, but not in mature neurons and oligodendrocytes (Figure 1A) (Kaneko et al. 2000; Dobson et al. 2008). In histological studies of neural and epithelial tissues, MSI1 is routinely used as a marker for stem and progenitor cells (Johnson et al. 2010). Analysis in mice and primary cells shows that MSI1 regulates neural development. *Msi1*$^{-/-}$ knockout mice are uncoordinated, ataxic, develop hydrocephaly, and die within 1-2 months after birth (Sakakibara et al. 2002). Their brains are small, contain an expansion of early lineage progenitor cells, and display fewer mature cell types than normal (Sakakibara et al. 2002). Embryonic neurospheres cultured from *Msi1*$^{-/-}$ mouse brains have a reduced capacity to differentiate into mature neurons and oligodendrocytes (Sakakibara et al. 2002). In primary oligodendrocyte progenitor cells, MSI1 promotes progenitor cell survival and prevents differentiation into mature oligodendrocytes (Dobson et al. 2008). The phenotype and expression pattern reveal that MSI1 plays an early role in regulating neurogenesis and gliogenesis.

MSI1 contains two RNA Recognition Motifs (RRMs) and is homologous to *Drosophila melanogaster* Musashi, a post-transcriptional regulatory protein that guides external sensory bristle patterning in flies (Sakakibara et al. 1996). *In vitro* SELEX experiments identified a series of aptamer sequences that bind to MSI1 (Imai et al. 2001). Visual inspection identified a consensus sequence (G/A)U_{1-3}AGU that was present in most but not all of the aptamers. A number of MSI1 targets have been identified by co-immunoprecipitation, including NUMB, a repressor of NOTCH signaling. *Numb*

transcripts harbor MSI1 consensus elements in the 3′-UTR (Imai et al. 2001). MSI1 interacts with the *Numb* 3′-UTR in vitro, and *Numb* mRNA co-immunoprecipitates with MSI1 in transiently transfected NIH 3T3 cells. Overexpression of MSI1 in NIH 3T3 cells decreases NUMB protein levels without affecting *Numb* mRNA and reduces the expression of a luciferase reporter in a 3′-UTR dependent manner (Imai et al. 2001). Together, the results show that MSI1 negatively regulates *Numb* mRNA translation. In contrast, MSI1 acts as a translational activator in *Xenopus laevis* oocytes, where it modulates cell cycle progression by regulating mRNA encoding the proto-oncogene Mos (Charlesworth et al. 2006).

MSI1 also promotes proliferation of numerous cancers of the brain and epithelial tissues (Toda et al. 2001; Hemmati et al. 2003; Yokota et al. 2004; Sanchez-Diaz et al. 2008; Sureban et al. 2008). MSI1 depletion in medulloblastoma and colorectal tumors results in decreased proliferation and increased apoptosis (Sanchez-Diaz et al. 2008; Sureban et al. 2008). In colorectal tumors, MSI1 depletion is accompanied by inhibition of Notch-1 and upregulation of $p21^{WAF1}$, a MSI1 target involved in cell cycle regulation (Battelli et al. 2006; Sureban et al. 2008). Musashi-2 (MSI2) is 69% identical to MSI1 protein and is expressed in a partially overlapping set of tissues (Sakakibara et al. 2002). MSI2 regulates hematopoesis and is involved in acute myeloid leukemia (Ito et al. 2010; Kharas et al. 2010). In myeloid leukemia cells, MSI2 is highly expressed, and depletion results in decreased proliferation and increased apoptosis (Kharas et al. 2010). The crisis phase of myeloid leukemia is marked by low NUMB expression (Ito et al. 2010). Loss of MSI2 restores NUMB expression and impairs the blast crisis phase of myeloid leukemia

(Ito et al. 2010). Ultimately, MSI2 expression levels are directly correlated with poor prognosis in myeloid leukemia patients (Kharas et al. 2010).

Because of the importance of Musashi family proteins in stem and cancer cell proliferation, we sought to identify a small molecule inhibitor of MSI1 RNA-binding activity. After screening more than 30,000 compounds, we identified four inhibitors, one of which is the intermediary metabolite oleic acid. Here we characterize the specificity and mechanism of oleic acid inhibition and identify a novel regulatory target that enables MSI1 to act as a metabolite sensor.

Results

Small molecule screen to identify inhibitors of Musashi-1

To screen for small molecule inhibitors of MSI1 RNA-binding activity, we developed an in vitro assay pipeline amenable to high throughput measurements. First, we tested the ability of a purified, his6-tagged MSI1 dual RRM construct (amino acids 7-192, Figure 1- figure supplement 1A) to bind a fragment of a previously identified SELEX aptamer (CCCR005) (Imai et al. 2001) using two quantitative assays: fluorescence electrophoretic mobility shift (F-EMSA) and fluorescence polarization (FP, Figure 1B-D) (Pagano et al. 2011). MSI1 binds with high affinity to the aptamer fragment, which contains two copies of the consensus sequence. Next, we optimized the FP assay for use in high throughput screens. We used this assay to screen two small molecule libraries: the 1280-compound Sigma Library of Pharmacologically Active Compounds (LOPAC) and the 30,000-compound Chembridge library (Figure 1E, 2A).

Inhibitors identified in the screen were validated by dose response measurements using both the FP and F-EMSA assays (Figure 1E-F).

Four candidate inhibitors were identified. The weakest inhibitor was the Chembridge compound 7409829 ($K_{i,\ app,\ FP}$ = 15 ± 2.8 μM, $K_{i,\ app,\ F\text{-}EMSA}$ = 54 ± 22 μM). The most potent inhibitor was aurintricarboxylic acid (ATA, $K_{i,\ app,\ FP}$ = 230 ± 30 nM, $K_{i,\ app,\ F\text{-}EMSA}$ = 1.55 ± 0.14 μM), a compound that readily polymerizes in aqueous solution to form a polyanion. This compound has been identified in many high throughput small molecule assays as a non-specific inhibitor of protein-nucleic acid interactions (Lam et al. 1995). The next inhibitor was GW7647, a PPARα agonist (Berger and Moller 2002). PPARα is a nuclear hormone receptor that is activated by long chain unsaturated fatty acids (Gottlicher et al. 1992; Bocos et al. 1995; Forman et al. 1997; Kliewer et al. 1997). The $K_{i,\ app}$ for this compound was 6.5 ± 0.4 μM by FP and 21 ± 0.8 μM by F-EMSA. The final inhibitor was oleic acid, an eighteen-carbon monounsaturated fatty acid with one double bond located nine carbons from the aliphatic—omega—end of the molecule (18:1, ω-9). The apparent K_i of this compound was 1.2 ± 0.4 μM by FP and 1.4 ± 0.7 μM by F-EMSA, and we observed decreased affinity for the RNA aptamer with increasing concentrations of oleic acid (Figure 1F, Figure 1-figure supplement 1B). The $K_{i,\ app}$ is approximately two orders of magnitude below the critical micelle concentration (CMC) in our equilibration buffer (pH 8.0) as measured by N-phenyl-1-naphthylamine (CMC ≥ 75 ± 8 μM, Figure 1-figure supplement 1C).

Oleic acid has been screened in 754 bioassays reported in the PubChem database. Of these, oleic acid scored as positive in 4% of the assays. It should be noted that this figure overestimates the hit rate because it includes multiple bioassays that target the

same protein. For example, oleic acid scored as a positive in eleven bioassays targeting fatty acid binding proteins (FABP) and seven assays that target membrane-associated potassium channels. Both are known to be sensitive to fatty acids (Capaldi et al. 2006; Boland and Drzewiecki 2008). Other proteins responsive to oleic acid include fatty acid synthase, estrogen synthase, factor VIIa complex, and enterotoxin. It also scored positive in a screen for membrane permeant biomolecules. In total, only 14 unique proteins are responsive to oleic acid. This suggests that oleic acid inhibition is specific.

MSI1 is specifically inhibited by 18-22 carbon ω-9 monounsaturated fatty acids

Oleic acid is the most abundant fatty acid in body fat and is produced by mature oligodendrocytes during myelination (Martinez and Mougan 1998). Cells can produce almost any fatty acid by modifying existing fatty acids through precise metabolic pathways. Because oleic acid is structurally related to a large number of fatty acids, we obtained a library of fatty acids and analogs to assess the specificity of inhibition (Figure 1F, Figure 2). First, we measured inhibition by longer omega-9 monounsaturated fatty acids using the FP and F-EMSA dose response assays. Eicosenoic acid (20:1, ω-9) inhibited MSI1 with a potency similar to oleic acid ($K_{i,\,app,\,FP}$ = 1.2 ± 0.4 μM, $K_{i,\,app,\,F\text{-}EMSA}$ = 1.7 ± 0.6 μM). Erucic acid (22:1, ω-9) was a stronger inhibitor ($K_{i,\,app,\,FP}$ = 640 ± 150 nM, $K_{i,\,app,\,F\text{-}EMSA}$ = 820 ± 30 nM), and nervonic acid (24:1, ω-9) inhibited more weakly ($K_{i,\,app,\,FP}$ = 47 ± 25 μM, $K_{i,\,app,\,F\text{-}EMSA}$ = 23 ± 8 μM). Second, we assessed truncations and modifications of the aliphatic end of the fatty acid. Removing two carbons (palmitoleic acid, 16:1, ω-7) had a moderate effect on inhibition ($K_{i,\,app,\,FP}$ = 5.3 ± 0.5 μM, $K_{i,\,app,\,F\text{-}EMSA}$ = 12 ± 0.9 μM). The presence of a hydroxyl group at carbon 12

(ricinoleic acid, 12-hydroxy-oleic acid) had a stronger effect; inhibition is barely detectable by FP and reduced 15-fold in F-EMSA measurements ($K_{i, app, F\text{-}EMSA} = 18 \pm 9$). Third, we assessed esterification or other modification of the carboxylate group. Oleamide, ethyl oleate, and 4-methylumbelliferyl oleate failed to inhibit RNA-binding. In contrast, the presence of a Coenzyme A (CoA) substituent was apparently tolerated, although we noted some deacylation of acyl-CoA stocks by thin layer chromatography. Fourth, we assessed the requirement for the ω-9 double bond. Stearic (18:0), palmitic (16:0), and myristic (14:0) acids failed to inhibit MSI1 RNA-binding activity, indicating that the ω-9 double bond is required. Surprisingly, the orientation of the double bond is also critical. Elaidic acid (18:1, ω-9 *trans*) has the same molecular weight as oleic acid, and nearly identical refractive index and molar aqueous solubility (~10 mM at pH 8.0), but its ω-9 double bond is *trans* rather than *cis*. Elaidic acid did not inhibit MSI1 (Figure 1F). Linoleic (18:2, ω-9, ω-6) and arachidonic (20:4, ω-12, ω-9, ω-6, ω-3) polyunsaturated fatty acids also inhibit MSI1, but with a weaker apparent inhibition constant (Linoleic acid: $K_{i, app, FP} = 2.2 \pm 0.2$ μM, $K_{i, app, F\text{-}EMSA} = 1.2 \pm 0.03$ μM; Arachidonic acid: $K_{i, app, FP} = 3.0 \pm 0.2$ μM, $K_{i, app, F\text{-}EMSA} = 1.1 \pm 0.3$ μM). We conclude that omega-9 *cis* unsaturated fatty acids between 18 and 22 carbons specifically inhibit MSI1 RNA-binding activity and identify erucic acid as the most potent inhibitor (Figure 2). MSI2 was inhibited with similar specificity (Figure 2-figure 2 supplement 1).

Oleic acid directly interacts with the RRM1 of MSI1 to effect inhibition

In principle, inhibitory fatty acids could inhibit by interacting with either MSI1 or its RNA target. We hypothesized that if the fatty acid bound to the RNA-binding domain

171 of MSI1, the interaction might alter the local environment of its single tryptophan (W29),
172 leading to a change in the intrinsic fluorescence (Vivian and Callis 2001). To test this
173 hypothesis, we titrated oleic acid or elaidic acid (trans-oleic acid) into recombinant MSI1
174 protein or an n-acetyl-L-tryptophanamide (NATA) control and measured tryptophan
175 fluorescence. Titration of oleic acid, but not elaidic acid, strongly quenched tryptophan
176 fluorescence and altered the emission intensity curve shape from 300 to 400 nm (Figure
177 3A, Figure 3-figure 3 supplement 1A-D). Neither compound affected the fluorescence of
178 NATA. In our buffer system, the maximal emission for both NATA and MSI1 is 350 nm
179 (Figure 3-figure 3 supplement 1A-D). We fit the emission at 350 nm to a quadratic,
180 bimolecular association model in order to determine the apparent dissociation constant.
181 The $K_{d, app}$ of oleic acid was 2.6 ± 1 μM, essentially identical to the $K_{i, app}$ determined by
182 FP and F-EMSA dose response experiments (Figure 2A, Figure 3A). Our data are
183 consistent with inhibition resulting from a direct association of oleic acid with the MSI1
184 protein.

185 The NMR structures of MSI1 RRM1 and RRM2 in the absence and presence of
186 RNA show that both domains adopt the canonical RRM fold in which an anti-parallel
187 beta sheet is buttressed by two alpha helices (Figure 3B) (Nagata et al. 1999; Miyanoiri et
188 al. 2003; Ohyama et al. 2011). In RRM domain proteins, the beta sheet surface typically
189 forms the RNA-binding platform (Figure 3B) (Kielkopf et al. 2004; Clery et al. 2008). In
190 the RNA-bound structure, several conserved amino acids located on the beta sheet
191 surface and loops make sequence-specific contacts to the RNA (Ohyama et al. 2011).
192 Notably, W29 directly contacts RNA by stacking on the first purine nucleotide. Our data
193 reveal that fatty acid binding causes W29 fluorescence quenching, suggesting that

194 binding changes the environment surrounding this amino acid. As such, fatty acid binding
195 may inhibit MSI1 RNA-binding by an allosteric mechanism.

196 To assess whether oleic acid association induces a change in MSI1 secondary
197 structure, we collected circular dichroism spectra as a function of fatty acid treatment.
198 We observe a decrease in mean residue ellipticity centered around wavelength 220 nm
199 upon treatment with oleic acid but not elaidic acid (Figure 3C, Figure 3-figure 3
200 supplement 1E). To determine whether the spectral changes correspond to a change in
201 oligomerization state, we performed velocity sedimentation analytical ultracentrifugation
202 experiments (Demeler et al. 2011). We observe no significant change in the velocity
203 sedimentation profile of MSI1 by van Holde-Weischet analysis after adding either oleic
204 acid or elaidic acid, and the predominant species remains monomeric (Figure 3D)
205 (Demeler and van Holde 2004; Demeler et al. 2011). We conclude that oleic acid binding
206 alters the secondary structure of MSI1, but this transition does not appear to induce
207 aggregation at concentrations below the CMC.

208 After examining the published NMR structures, we were intrigued to note a
209 hydrophobic cavity on the alpha-helical surface of RRM1, opposite the RNA-binding
210 surface (Figure 3B) and adjacent to W29 (Nagata et al. 1999; Miyanoiri et al. 2003).
211 MSI1 RRM2 does not have this feature. We hypothesized that this cavity comprises the
212 fatty acid binding site. To test this idea, we first asked whether RRM1 is sufficient for ω-
213 9 fatty acid inhibition. We purified his6-tagged MSI1 RRM1 (amino acids 7-103) and
214 used FP and F-EMSA to determine whether RRM1 is sufficient for both RNA binding
215 and inhibition by oleic acid. RRM1 bound to the aptamer RNA with an apparent K_d of
216 75.2 ± 10 nM by FP (Figure 3-figure 3 supplement 2A). Addition of oleic acid but not

217 elaidic acid inhibits RNA-binding activity with similar $K_{i, app}$ compared to the full RNA-
218 binding domain (Figure 3-figure 3 supplement 2B). Thus, RRM1 is sufficient for RNA
219 recognition and fatty acid inhibition.
220 Next, we prepared a ^{15}N labeled sample of RRM1 for NMR spectroscopy,
221 collected an ^{15}N-^{1}H HSQC spectrum, and titrated aptamer RNA to identify amide proton
222 chemical shift differences associated with RNA binding (Figure 3-figure 3 supplement
223 2C). The majority of the chemical shift differences map to the β-sheet surface and the
224 loops, which is typical for RRM proteins. Notably, backbone amide protons
225 corresponding to F23, G64, and F65, display large chemical shift changes upon RNA
226 binding. In contrast, chemical shifts changes on the α helical face are small. The data
227 are consistent with the model where the β-sheet surface recognizes RNA, and that
228 binding involves a structural transition including F23, G64, and F65 (Ohyama et al.
229 2011). Next, we titrated oleic acid or elaidic acid into the sample of MSI1 (Figure 3-
230 figure 3 supplement 2D-F). We expected to observe chemical shift changes associated
231 with oleic acid binding to the protein. The addition of increasing amounts of oleic acid
232 did not result in significant changes in chemical shifts but in considerable reduction of the
233 peak intensities and in line broadening. The largest loss of signal upon addition of
234 substoichiometric concentrations of oleic acid was observed for W29, Q30, L36, C49,
235 L50, R53, S60, G62, V74, T89, and K98 (Figure 3, Figure 3-figure 3 supplement 2E-F).
236 The observed loss of signal is likely due to chemical exchange between the free and
237 bound state. As expected, we detected a strong loss in signal intensity across the entire
238 protein when the concentration of oleic acid exceeded the CMC (75 ± 8 μM, Figure 1-
239 figure 1 supplement 1C and Figure 3-figure 3 supplement 2D-F). The observed general

loss of MSI1 signal is probably due to precipitation of the protein-oleic acid complex, or it could be attributed to the interaction of MSI-1 with oleic acid micelles, or both. We note that a precipitant forms in the NMR tube at elevated oleic acid concentration. Because the CMC of oleic acid is below the concentration needed to make a saturated MSI1 sample (Figure 1-figure 1 supplement 1C), we cannot form sufficient MSI1-oleic acid complex for NMR structural studies.

A model of the omega-9 fatty acid inhibition mechanism

Because the high concentrations needed for NMR spectroscopic studies precluded direct measurement of the MSI1 fatty acid interface, we performed computational docking calculations with eicosenoic acid or oleic acid with MSI1 RRM1 (Figure 2, Figure 4) (Friesner et al. 2004; Friesner et al. 2006). In the docked models, both compounds insert the ω-9 end into the cavity, form extensive contacts with the protein surface, and position their carboxy termini adjacent to a positively charged arginine side chain (R53 or R61, dependent on the model, Figure 4A-B, Figure 3-figure 3 supplement 2D-F, Figure 4-figure 4 supplement 1A). The docked model explains the specificity of inhibition. Amide and ester derivatives lose the negative charge and cannot form charge-charge interactions with arginine (oleamide, ethyl oleate). Shorter omega-7 fatty acids will not fill the hole (palmitoleic acid). Modifications of the omega end limit insertion into the hole (ricinoleic acid). Eighteen carbons enable the carboxylate to reach R53 (oleic acid), (Figure 4A-B, Figure 4-figure 4 supplement 1A). Twenty-four carbons position the group beyond the arginine (nervonic acid). Trans orientation of the double bond limits surface contact and prevents orientation of the carboxylate towards R53

263 (elaidic acid). Finally, saturation of the double bond would require a large entropic
264 penalty in order to adopt the necessary conformation (stearic acid).

265 To further assess how fatty acid binding alters the dynamics of amino acids that
266 contribute to RNA recognition, we performed molecular dynamics (MD) simulations of
267 the MSI1 RRM1 motif with and without oleic acid. The NMR structure of MS1 RRM1
268 served as the starting configuration for the free state (Nagata et al. 1999; Miyanoiri et al.
269 2003). Three different models derived by docking oleic acid provided the starting
270 configurations for the oleic acid-bound state (Friesner et al. 2004; Friesner et al. 2006).
271 Each of the four simulations was equilibrated for 1 ns and data were collected during a
272 subsequent 30 ns trajectory. Upon oleic acid binding, MSI1 underwent a transition to a
273 more open state characterized by an increase in solvent accessible surface area (SASA)
274 and radius of gyration (Figure 5A). Direct visualization of the structure's time evolution
275 showed that binding of oleic acid is associated with stabilization of the C-terminus of α-
276 helix 1, fraying of α-helix 2 at both the N- and C-termini and, in one trajectory, formation
277 of an additional β-sheet in loop 5 (Figure 4C-D, Movie 1). The computed probability of
278 each residue to be in a secondary structural element (Figure 5C) supports our
279 observations. Notably, the β-sheet that forms in loop 5 is absent in the MSI1 apo
280 structure but is present in the structure of MSI1 bound to RNA (Figure 4D) (Ohyama et
281 al. 2011).

282 Analysis of the structure and dynamics of MSI1 bound to oleic acid and its
283 comparison to the RNA-bound structure suggests a mechanism of inhibition. Oleic acid
284 binding stabilizes β-strand formation in loop 5 and alters its position relative to helix 1.
285 The distance between the C-terminus of α-helix 1 and loop 5 in the free and oleic acid-

286 bound state is greater than that observed in the RNA-bound state (Figure 4D, Figure 5).
287 The presence of oleic acid blocks loop 5 from approaching the C-terminus of α-helix 1.
288 When loop 5 is in the more open conformation, K88 is not in position to interact with the
289 first purine nucleotide of the consensus, in this case Gua1. In addition, binding of oleic
290 acid causes W29 to stack against the side chain of Q30. (Figure 4E-F, Figure 5). This
291 observation is in agreement with the NMR signal intensity loss observed for certain
292 residues during oleic acid titration (Figure 3-figure 3 supplement 2D-F), as well as the
293 strong quenching of MSI1 tryptophan fluorescence measured upon addition of oleic acid
294 (Figure 3A, Figure 3-figure 3 supplement 1A-D). W29 directly stacks with the first RNA
295 nucleotide, stabilizing the interaction between MSI1 and RNA. Stacking is eliminated in
296 the presence of oleic acid (Figure 4E-F). Finally, strand 4 is more flexible in the oleic
297 acid-bound state than in free MSI1 (Figure 4E-F). Strand 4 contains several residues that
298 directly contact RNA. The simulations suggest that oleic acid weakens these interactions.
299 In contrast to our initial hypothesis, we do not observe a dramatic change in the dynamics
300 of F65 in the presence of oleic acid over the time course of the simulations.
301 The circular dichroism and analytical ultracentrifugation data (Figure 3C-D,
302 Figure 3-figure 3 supplement1E) are consistent with a net gain in secondary structure
303 upon oleic acid binding, as predicted by the MD simulation (Figure 4, Figure 5). In
304 addition, the change in tryptophan fluorescence observed upon oleic acid but not elaidic
305 acid treatment is consistent with the changes in tryptophan solvent exposure observed in
306 the simulation.
307 To test features of the model, we mutated residues predicted to interact with oleic
308 acid (Figure 4-figure 4 supplement 1) and measured the relative inhibition constant ($K_{rel,}$

309 $_{app}$) by dose response FP. We observed no change in fatty acid inhibition when Q30 was
310 mutated to a glutamate ($K_{rel, app}$ = 0.9, Figure 4 Supplement 1). Mutation of H83 to
311 leucine also had no effect on fatty acid inhibition. Mutation of H83 to phenylalanine
312 reduced inhibition by almost 2-fold. H83 lines the hydrophobic pocket. Mutation of this
313 residue to phenylalanine is predicted to make the pocket narrower. Mutation of G64 to
314 alanine reduced inhibition by 3.1 fold. G64 forms the floor of the hydrophobic pocket,
315 mutation to an alanine is expected to make the pocket more shallow. Mutation of G35 to
316 aspartate and glutamate results in a 2-fold and 7-fold reduction of inhibition, respectively.
317 This is possibly due to the to the addition of a negative charge near the mouth of the
318 hydrophobic cavity.
319 To test whether the R53 and/or R61, which are predicted to interact with the
320 carboxylate end of oleic acid, are important for inhibition, we made single glutamate
321 mutations at each position (R53E or R61E). Oleic acid inhibition of the R53E mutant is
322 reduced 3-fold, while R61E is reduced 5-fold. Mutating both arginines (R53E/R61E)
323 increases this effect to 35-fold. This indicates that R53 and R61 are both important for
324 inhibition, and act in a partially redundant way. A triple mutant (R53E/R59E/R61E)
325 weakens inhibition by a similar amount (27-fold). The R53E mutant has a small effect on
326 RNA-binding, while the R61E mutant has a strong 18-fold effect. The interaction of R61
327 with oleic acid would preclude its interaction with RNA, and thus may contribute to the
328 mechanism of inhibition.
329 Together, the MD simulations and experimental data are consistent with an
330 allosteric model of inhibition, wherein fatty acid binding induces a change in
331 conformation that modifies the secondary structure of RRM1 and perturbs the position of

amino acids required for RNA recognition. Additional work will be necessary to determine whether fatty acid inhibition works via the mechanism suggested by the computational docking and MD simulations or through an alternative mechanism.

Oleic acid treatment reduces oligodendrocyte progenitor cell proliferation

To study the role of fatty acids in regulating MSI1 in a cell culture model, we investigated the effect of treating the immortalized rat oligodendrocyte progenitor cell line CG-4 with oleic acid (Louis et al. 1992). CG-4 cells maintain normal precursor cell morphology, can be readily transfected, and can be induced to differentiate into mature oligodendrocytes by withdrawal of growth factors (Franklin et al. 1995) (Louis et al. 1992). Mature oligodendrocytes produce myelin, a lipid-rich membrane structure that insulates neuronal axons to both protect them and to aid in saltatory impulse conductance throughout the CNS (Griffiths et al. 1998). The lipid and fatty acid profiles of mature oligodendrocyte-rich white matter differ from that of the grey matter (Martinez and Mougan 1998). CG-4 cells also shift lipid profiles upon differentiation, as detected by quantitative lipidomics mass spectrometry (Figure 6-figure 6 supplement 1). As with primary OPCs, MSI1 is expressed strongly in the precursor state but decreases upon differentiation (OPCs: 1.0 ± 0.3, oligodendrocytes: 0.15 ± 0.01, p-value = 0.0035). Treatment of CG-4 OPCs with oleic acid strongly inhibited the rate of cell proliferation (Figure 6), matching the published phenotype of MSI1 knock down in primary OPCs (Dobson et al., 2008). In contrast, treating HEK293T cells—which do not express MSI1—with the same concentration of oleic acid had little or no effect on the rate of proliferation. Treatment with stearic acid, which does not inhibit MSI1, had no effect on

355 proliferation rate in either cell type (Figure 6A). The data suggest that reduction of MSI1
356 activity by oleic acid limits proliferation, but we cannot rule out that the fatty acid
357 modulates other cellular pathways that contribute to proliferation.
358
359 *MSI1 regulates stearoyl-CoA desaturase*
360 We hypothesized that MSI1 might control the expression of enzymes required to
361 make long chain monounsaturated fatty acids. In humans, non-dietary oleic acid is
362 produced from stearic acid by stearoyl-CoA desaturase (SCD). Expression of SCD is
363 tightly controlled at the transcriptional, post-transcriptional, and post-translational levels.
364 In rodents, there are four SCD genes, *Scd1-4*. We used FP and F-EMSA assays to test the
365 ability of recombinant MSI1 to bind each of seven putative consensus sites present in the
366 *Scd1* 3'-UTR (Figure 6B). MSI1 binds to all seven sites by FP and F-EMSA (Figure 6-
367 figure 6 supplement 2). Site 2 and site 7 bind to MSI1 with comparable affinity to the
368 selected aptamer. The slightly decreased binding affinity measured for these 7 fragments
369 is likely due to the fact that our aptamer CCCR005 contains two MSI1 binding sites,
370 while each *Scd1* 3'-UTR fragment contains only a single MSI1 binding site. Transcripts
371 encoding SCD1 co-immunopreciptated with MSI1 from CG-4 cell extracts using two
372 independent antibodies (Figure 6-figure 6 supplement 2C). Similar results were obtained
373 with *Numb* mRNA, a positive control. Overexpression of MSI1 in HEK293T cells, which
374 do not endogenously express MSI1, increased the amount of SCD and SCD proteolysis
375 products by 2.5 ± 0.35 fold (p-value = 0.018, Figure 6D, Figure 6-figure 6 supplement
376 2B). We were unable to detect SCD expression in the rat CG-4 cells using available
377 antibodies. qRT-PCR analysis of HEK293T mRNA shows a slight but non-significant

increase in SCD1 transcript abundance upon MSI1 overexpression (Figure 6-figure 6 supplement 2C).

Next we sought to assay downstream effects of SCD regulation by MSI1 in cells. We reasoned that because SCD plays an integral role in lipogenesis, changes in SCD activity would result in a shift in the cellular lipid profile. To this end, we performed quantitative lipidomics mass spectrometry analysis. CG-4 cells proliferation halts upon MSI1 knockdown [Dobson, 2008 #6]. For this reason we performed these experiments in HEK293T cells with and without MSI1 expression. We observed statistically significant changes ranging from 2 to 32-fold in 54 of the 312 lipids assayed (FDR = 0.05, Figure 6E-F). We noted positive changes in 50 of 54 significant data points, indicating that MSI1 expression stimulates production of certain lipids. 38 of the significantly changing lipids fell into one of three cholesterol and triacylgylcerol (TAG) classes: cholesterol esters, 16:0 acyl-containing TAG, and 16:1 acyl-containing TAG (Figure 6G-H). Cholesterol esters and TAGs are made using SCD products, and have been shown to be more abundant in mice overexpressing SCD1, and less abundant in liver SCD1 knockout mice (Miyazaki et al. 2000; Attie et al. 2002). This indicates that SCD activity is upregulated in the presence of MSI1. Together, our binding data, co-immunoprecipitation, western blots, and lipidomics profiling results show that stearoyl-CoA desaturase expression is increased in the presence of MSI1, possibly through direct association with consensus motifs in the 3'-UTR of SCD transcripts. We note that of 2107 annotated 3' UTRs for genes involved with lipid, cholesterol, fatty acid biosynthesis, and SREBP activity, 1275 contain at least one MSI1 binding element. While the presence of a binding element does not confer regulation, MSI1 regulation of

lipid metabolism may be more complex than simple direct regulation of SCD. Indeed, a survey of 64 genes that associate with MSI1 in a RIP-ChIP experiment reveals that 8 are annotated to be involved with lipid metabolic processes [de Sousa Abreu, 2009 #435].

DISCUSSION

Our data reveal that the long chain ω-9 fatty acids oleic acids between 18-22 carbons in length are allosteric inhibiters of MSI1 RNA binding activity. Our data also show that SCD, the enzyme that catalyzes the ω-9 desaturation, is a MSI1 regulatory target. The results are consistent with a model where MSI1 controls cellular proliferation through a feedback loop that includes SCD and its enzymatic products, such as oleic acid (Figure 7).

Oleic acid is the precursor for synthesis of longer chain fatty acids such as eicosanoic, erucic, and nervonic acid, signaling molecules such as arachidonic acid, endocannabinoids, and prostaglandins, and membrane phospholipids. Oleic acid is abundant in the lipid-rich myelin membranes produced by mature oligodendrocytes (Martinez and Mougan 1998), and CG4 OPCs show global changes in the lipid profile upon differentiation. OPCs express MSI1, but mature myelinating oligodendrocytes do not (Dobson et al. 2008). In the oligodendrocyte lineage, oleic acid and MSI1 levels are anti-correlated, which suggests a possible biological role for MSI1 inhibition by fatty acids (Martinez and Mougan 1998; Dobson et al. 2008). Another MSI1 inhibitor identified in our screen was the PPARα agonist GW7647. PPARs are nuclear hormone receptor proteins that regulate cellular processes including fatty acid metabolism, differentiation, cell cycling, and inflammation (Berger and Moller 2002). PPARγ agonists

accelerate oligodendrocyte maturation (De Nuccio et al. 2011). Both GW7647 and oleic acid function as PPAR agonists, and both inhibit MSI1 RNA-binding activity, suggesting that MSI1 and PPARs possibly regulate gene expression in a reciprocal fashion.

We have identified the metabolic enzyme SCD as regulatory target of MSI1. The two human isoforms of SCD, SCD1 and SCD5, catalyze the conversion of saturated fatty acids (SFAs) into monounsaturated fatty acids (MUFAs) (Zhang et al. 1999; Beiraghi et al. 2003; Minville-Walz et al. 2010). MUFAs are then used in the synthesis of numerous lipids, including phospholipids, di- and triacylglycerols, cholesterol esters, and signaling molecules such as eicosanoids. SCD is therefore an essential enzyme to normal cellular proliferation, metabolism, and signaling. It is also possible that MSI1 may also be regulating other factors involved in lipid, fatty acid and cholesterol metabolism. The Penalva group identified 64 putative MSI1 targets using a RIP-ChIP analysis in HEK293T cells (de Sousa Abreu et al. 2009). Of these putative targets, eight are annotated to play a role in lipid, fatty acid or cholesterol metabolic processes. These include three variants of the fatty acid elongase ELOVL5, two variants of the glycolipid biosynthetic factor PIGF, two variants of Lamin B receptor (LBR), and aminoadipate-semialdehyde dehydrogenase-phosphopantetheinyl transferase (AASDHPPT).

SCD has been implicated in a number of disease states, including obesity, diabetes, hyperlipidemia, and cancer. Obese and diabetic animals produce abnormally high levels of TAGs and cholesterol esters (Coleman and Lee 2004). These energy storage molecules are also elevated in a hyperlipidemia mouse model that overexpresses SCD (Attie et al. 2002). Conversely, SCD1 knockout mice display impaired biosythesis of both TAGs and cholesterol esters (Miyazaki et al. 2000). SCD is upregulated in tumor

447 cells, including colonic and esophageal carcinoma (Li et al. 1994). Cancerous cells use
448 newly synthesized lipids primarily for phospholipid production, which are used in new
449 membranes (Swinnen et al. 2000). Additionally, new evidence suggests that SCD1
450 activates the oncogenic Akt and AMPK signaling pathways (Scaglia and Igal 2008;
451 Scaglia et al. 2009).

452 SCD regulates SFA and MUFA homeostasis, and therefore plays an integral role
453 in lipid signaling pathways. SFAs serve as proinflammatory factors by acting as ligands
454 for immune receptors such as those in the Toll-like receptor family (Shi et al. 2006;
455 Nguyen et al. 2007). MUFA products of SCD are further modified to become
456 polyunsaturated fatty acids, such as arachidonic acid, which are converted into
457 eicosanoids by cyclooxygenases (James et al. 2000). Eicosanoids serve as
458 proinflammatory and immune signaling molecules (Liu et al. 2011). Recent data also
459 links SCD to Wnt signaling through mediation of the palmitic/palmitoleic acid
460 conversion, as active Wnt proteins require conjugation of palmitoleic acid (Rios-Esteves
461 and Resh 2013). The balance between SFAs and MUFAs must be tightly controlled, and
462 while SCD is not the only enzyme involved in the process, it does serve as an essential
463 gatekeeper in the conversion of dietary SFA to MUFA.

464 Several examples of functional interactions between transcription factors and fatty
465 acids have been published. For example, fatty acids associate with membrane-bound
466 sterol responsive element binding protein (SREBP) to inhibit a cleavage event that
467 produces the activated form of SREBP, a transcription factor involved in lipid
468 homeostasis (Wang et al. 1994). Free fatty acids have been shown to stimulate
469 proinflammatory cytokine expression while decreasing anti-inflammatory cytokine

expression in adipocytes (Bradley et al. 2008). Interestingly, treatment of various tumor lines with oleic acid results in transcriptional inhibition of the Her-2/*neu* (*erb*B-2) oncogene through PEA3, although the precise mechanism of regulation remains unknown (Menendez et al. 2006). In yeast cells, fatty acids bind oleate-activated transcription factors (OAFs) to effect transcription of genes responsible for fatty acid metabolism, glucose metabolism, stress response, and other related processes (Gurvitz and Rottensteiner 2006). Although numerous transcription factors are regulated by fatty acids, to our knowledge, MSI1 is the first example of a fatty acid-responsive RNA binding protein.

Integration of metabolite sensing and post-transcriptional regulation is widespread in bacteria, but relatively few examples have been found in eukaryotes (Winkler and Breaker 2003; Roth and Breaker 2009). Riboswitches regulate gene expression at the RNA level in response to intermediary metabolites. Small molecule metabolites bind mRNA transcripts, usually in the 5' UTR, to induce a structural change that interferes with the transcriptional or translational machinery (Winkler and Breaker 2005). In bacteria, riboswitches sensitive to a number of metabolites have been characterized, including guanine, adenine, coenzyme B12, glycine, lysine, and thyamine pyrophosphate (TPP), among others (Grundy et al. 2003; Mandal et al. 2003; Sudarsan et al. 2003; Vitreschak et al. 2003; Mandal and Breaker 2004; Mandal et al. 2004). Although most riboswitches have been identified within the bacterial mRNA 5′ UTR, TPP riboswitches, have also been identified in plants and fungi (Kubodera et al. 2003; Sudarsan et al. 2003). While riboswitches comprise an essential cis-regulatory mechanism in bacteria, other

492 mechanisms of coupling metabolic state to post-transcriptional gene regulation may occur
493 in eukaryotes.

494 An increasing number of protein-metabolite-RNA interactions have now been
495 identified in bacteria and eukaryotes. One example is the *bacillus subtilis* tryptophan
496 RNA-binding attenuation protein (TRAP). Increasing intracellular tryptophan levels
497 induce TRAP multimerization, which enables mRNA recognition and subsequent
498 translational repression of targets (Gollnick et al. 1990; Antson et al. 1995; Babitzke et al.
499 1995; Yakhnin et al. 2004). Intriguingly, several metabolic enzymes have been proposed
500 to "moonlight" as RNA-binding proteins in "RNA / Enzyme / Metabolite (REM)"
501 networks (Ciesla 2006; Hentze and Preiss 2010; Castello et al. 2012). A notable example
502 is cytosolic aconitase, which demonstrates mutually exclusive enzymatic and RNA-
503 binding functionality, depending upon cellular iron levels (Hentze and Argos 1991;
504 Rouault et al. 1991). A number of metabolite-sensitive enzymes have also demonstrated
505 RNA-binding activity, including GAPDH, glutamate dehydrogenase, thymidylate
506 synthase, and dihydrofolate reductase (Ryazanov 1985; Chu et al. 1991; Chu et al. 1993;
507 Preiss et al. 1993; Dollenmaier and Weitz 2003). This growing body of research suggests
508 that metabolite-mediated post-transcriptional regulation is much more prevalent than
509 previously thought.

510 Our results show that MSI1 N-terminal RRM1 acts as a metabolite sensor, the
511 first example of such activity observed for the most abundant RNA-binding motif in
512 eukaryotic genomes. A survey of RRM structures in the protein data bank reveals several
513 with a surface cavity on the alpha helical face, which may comprise metabolite-binding
514 pockets. We predict that a network of RNA regulatory proteins act as metabolite sensors,

possibly replacing the bacterial riboswitch regulation that appears to have been largely lost in eukaryotes.

Experimental Procedures

Plasmids

DNA encoding the mouse MSI1 RNA binding domain fragment (amino acids 7-192) was amplified from the mammalian gene collection (MGC) full-length ORF clone 100014969 (Invitrogen) using gene specific primers (forward primer: 5'-cgcgcggatcccagcccggcctcgcctcccc-3'; reverse primer: 5'-gcgcgaagcttcggggacatcacctcctttg-3'). This fragment was digested using BamHI and HindIII restriction enzymes and subcloned into a modified version of pET-22b vector (Invitrogen) in which the pelB leader sequence was replaced with a His6-Gly tag followed by a TEV protease site to make pET-22HT-MSI1 (7-192). Mutant versions of the MSI1 RNA binding domain were prepared by site-directed mutagenesis using QuikChange (Stratagene). The human MSI2 RNA binding domain fragment (amino acids 8-193) was amplified from MGC full-length ORF clone 3505639 using gene specific primers (forward primer: 5'-cgcgcggatccggcacctcgggcagcgccaa-3'; reverse primer: 5'-gcgcgaagctttcatgggaacatgacttctttcg-3'). This fragment was cloned into the BamHI and HindIII restriction sites of pET-22HT to make pET-22HT-MSI2 (8-193). The MSI1 RRM1 plasmid pET-22HT-MSI1 (7-103) was prepared by site-directed mutagenesis using QuikChange (Stratagene) to replace M104 with an ochre stop codon. Full-length mouse MSI1 was amplified from MGC full-length ORF clone 100014969 (Invitrogen) using forward primer 5'-cgcgcggatccatggagactgacgcgcccca-3' and reverse primer 5'-

ccgggcggccgctcagtggtacccattggtgaa-3'. The resulting fragment was subcloned into pCDH-CMV-MCS-EF1-Puro (System Biosciences) using the BamHI and NotI restriction enzymes to make pCDH-CMV-MSI1(FL).

Purification of recombinant proteins

H6-TEV-MSI-1 (7-192), H6-TEV-MSI-1 (7-104), and H6-TEV-MSI-2 (8-294) were expressed and purified from *Escherichia Coli* BL21(DE3) cells. Liquid cultures grown at 37ºC were induced for 3 hours during mid-log phase with 1 mM Isopropyl β-D-1-thiogalactopyranoside (IPTG). Cells were pelleted, resuspended in lysis buffer (50 mM NaH_2PO_4, 300 mM NaCl, 20 mM Imidazole, 5 mM β-Mercaptoethanol (BME)), and lysed using a microfluidizer (IDEX Health and Science). Soluble lysate was applied to a Ni-NTA column (Qiagen), washed with wash buffer (50 mM NaH_2PO_4, 300 mM NaCl, 50 mM Imidazole, 5 mM BME), and eluted with elution buffer (50 mM NaH_2PO_4, 300 mM NaCl, 300 mM Imidazole, 5 mM BME). Fractions were analyzed by SDS-page and those containing recombinant MSI1 or MSI2 were pooled and dialyzed overnight into S buffer (50 mM MOPS pH 6.0, 20 mM NaCl, 2 mM DTT). Pooled fractions were applied to a HiTrap SP cation exchange column (GE Healthcare) and eluted using a gradient of 0.1M to 1 M NaCl in S Buffer. Fractions containing MSI1 or MSI2 were pooled and dialyzed overnight into Q buffer (50 mM Tris pH 8.8, 20 mM NaCl, 2 mM DTT) prior to loading a HiTrap Q anion exchange column (GE Healthcare). The protein was eluted over a gradient from 0.1 to 1 M NaCl in Q buffer. Fractions containing MSI were pooled and dialyzed using Spectra/Por 7 25 kD (MSI1) or 10 kD (MSI2) molecular weight cutoff tubing (Spectrum laboratories) overnight into storage buffer (50 mM Tris pH 8.0, 20 mM

NaCl, 2 mM DTT). The yield of >95% pure MSI1 or MSI2 is typically 20 mg per liter of culture (Figure 1-figure 1 supplement 1).

RNA sequences and labeling

Synthetic RNA oligonucleotides were ordered from IDT and 3' end-labeled with fluorescein 5-thiosemicarbazide (Invitrogen) according to the method of Reines and Cantor (Reines and Cantor 1974; Pagano et al. 2007; Farley et al. 2008). Briefly, $5x10^{-10}$ mol of RNA were incubated with 100 mM NaOAc, pH 5.1 and 5 nmol of NaIO4 for 90 minutes at room temperature then ethanol precipitated. The RNA was resuspended in 50 µl of 1 mM fluorescein-5-thiosemicarbazide in 100 mM NaOAc, pH 5.1. After incubating overnight at 4 °C, the RNA was separated from unreacted label by ethanol precipitation and subsequently passaged through a Pierce centrifuge column packed with Spehadex G-25 resin (GE Healthcare). RNA CCCR005 was a truncated form of the SELEX aptamer S8-13 identified by the Okano lab (Imai et al. 2001). In preparation for the small molecule screen, fCCCR005 (AGCGUUAGUUAUUUAGUUCG/36-FAM/) was ordered pre-labeled from IDT.

Fluorescence polarization and electrophoretic mobility shift assays

Fluorescence polarization (FP), also known as fluorescence anisotropy, and Fluorescence electrophoretic mobility shift assays (F-EMSA) were used to measure the binding affinity of recombinant MSI1 to fluorescein-labeled RNA aptamers. Assays were conducted as described in Pagano, et al. (Pagano et al. 2011). Briefly, 2 nM fluorescein-labeled RNA was incubated with varying concentrations of recombinant purified MSI1 protein in

equilibration buffer (37.5 mM Tris pH 8.0, 75 mM NaCl, 0.0075% igepal, 0.0075 mg/mL tRNA) for three hours. Fluorescence polarization was determined with a Victor V3 plate reader using a 480 ± 31 nm excitation filter and a 535 ± 40 nm emission filter. After measuring FP, the samples were mixed with 6x bromocresol green loading dye (0.15% (w/v) Bromocresol green, 30% (v/v) glycerol) and run on a 5% native polyacrylamide gel at 120V for 75 minutes at 4ºC. Wet gels were scanned with a Typhoon FLA 9000 Biomolecular imager (GE healthcare) using a 473 nm laser and a long-pass cut-off filter (510 nm). The fraction of bound RNA was determined by quantifying lower (free) and upper (bound) band intensities using MultiGauge and ImageGauge software (Fujifilm). For RNA sequences with two shifted species, the bands were quantified together.

Polarization values or the fraction of bound RNA were plotted as a function of protein concentration and fit to the Hill equation (1) to determine the apparent dissociation constant (K_d) and the apparent Hill coefficient (n). The upper (m) and lower (b) values were also fit in order to define the assay window.

$$\phi = b + (m - b)\left\lfloor \frac{1}{1 + \left(K_d / [P_t]\right)^n} \right\rfloor \quad (1)$$

For RNA sequences where a bi-phasic transition was observed, the FP data were fit using a two-site model (equation 2) to determine both apparent dissociation constants (K_{d1} and K_{d2}) and the fraction (F) of signal that corresponds to each transition.

$$\phi = \left[F(m-b)\left(\frac{P_t}{P_t - K_{d1}}\right)\right] + \left[(1-F)(m-b)\left(\frac{P_t}{P_t + K_{d2}}\right)\right] + b \qquad (2)$$

Small molecule screen

The small molecule screen was performed at the UMass Medical School small molecule screening core facility using a variation of the FP assay described above. 100 nM recombinant MSI1 protein and 2 nM fluorescein-labeled RNA aptamer CCCR005 were added to each assay well of 384-well black plates (Corning) using a μFill liquid dispenser (BioTek). Compounds dissolved in DMSO from the LOPAC and Chembridge libraries of small molecules were spotted in each assay well to a final concentration of 384 μM using a Tecan genesis workstation 150. Sixty-four wells of each plate were reserved for controls, including thirty-two wells that included no protein and no compound (free RNA), and 32 wells that included protein, RNA, and DMSO (no compound). Plates were equilibrated at 25ºC prior to collecting polarization and fluorescence intensity data for each well using a Victor V2V plate reader (Perkin Elmer). The Z' score, a measure of signal-to-noise, was calculated for each plate using the average (μ) and standard deviation (σ) of the control wells (equation 3).

$$Z^1 = 1 - \left[\frac{3(\sigma_1 + \sigma_2)}{\mu_1 - \mu_2} \right] \qquad (3)$$

Plate reads with a Z' of < 0.5 were repeated. The average Z' of all plates was 0.7 ± 0.2. The polarization values (mP) of each well were normalized against the assay window

using the mean polarization values of the no protein control (μ_2) and no compound control (μ_1) wells to generate an assay score (equation 4).

$$Score = \frac{mP - \mu_2}{\mu_1 - \mu_2} \quad (4)$$

Hits were classified as wells with a score of 0.1 or less where the fluorescence intensity remained within 2-fold of the control average to eliminate false positives due to compound fluorescence or quenching.

Dose response experiments

Dose response experiments to assess inhibition activity were performed using a modified FP and F-EMSA protocol. A constant concentration of sub-saturating protein was equilibrated with 2 nM fluorescein-labeled RNA and varying concentrations of compound in equilibration buffer. The FP and F-EMSA data were collected as above and fit to a sigmoidal dose response equation to determine the IC50 (equation 5).

$$\phi = b + (m - b)\left\lfloor \frac{1}{1 + \left(IC_{50} / [P_t]\right)^n} \right\rfloor \quad (5)$$

The apparent inhibition constant was calculated using the Lin and Riggs conversion (equation 6), which corrects for the equilibrium dissociation constant of MSI1 for the

646 labeled RNA as well as the concentration of labeled RNA and protein used in the
647 experiment (Lin and Riggs 1972; Ryder and Williamson 2004).
648
649 $$K_{i,app} = \frac{2(K_d)(IC_{50})}{2P - R - 2K_d} \quad (6)$$
650
651 **Intrinsic tryptophan fluorescence assay**
652 To directly assay the association of fatty acids and MSI1 protein, 6 μM MSI1 or N-
653 acetyl-tryptophanamide (NATA) was incubated with varying concentrations of
654 compound. Equilibrated reactions were excited at 280 nm, then steady-state fluorescence
655 emission spectra were recorded between 295 and 400 nm in one nm intervals using a T-
656 format Fluorolog fluorimeter (Horiba). 350 nm emission data were normalized and fit to
657 a quadratic bimolecular association curve (equation 7) to determine the apparent
658 dissociation constant, where C is the total compound concentration, P is the total protein
659 concentration, and m and b represent the maximal and minimal signal, respectively.
660
661 $$\phi = b + (m - b)\left[\frac{C + P + K_d - \sqrt{(C + P + K_d) - 4(CP)}}{2C}\right] \quad (7)$$
662
663 **In-silico Docking analysis**
664 The ligand molecules were downloaded from the PubChem database
665 (pubchem.ncbi.nlm.nih.gov) and prepared for docking using the LigPrep module in
666 Maestro (Schrödinger, LLC). The target protein structures were downloaded from the

667 PDB (www.rcsb.org) and prepared for docking in Maestro (Schrödinger, LLC) using the
668 Protein preparation wizard. Glide (Schrödinger, LLC) was used to generate the receptor
669 grid for subsequent docking and scoring the docked ligands in Standard Precision (SP)
670 mode. The pose with best Glide score from each ligand/receptor docking run was selected
671 for further analysis (Friesner et al. 2004; Halgren et al. 2004; Friesner et al. 2006).
672
673 **NMR**
674 Labeling with ^{15}N was performed by growing cells in isotopically enriched M9 medium,
675 1g $^{15}NH_4Cl$ per liter. 2D ^{1}H-^{15}N HSQC spectra were collected using samples of U-^{15}N
676 MSI1 in 90% H_2O/10%D_2O buffer solution of 50 mM Tris at pH 7.0. 2D ^{1}H-^{15}N HSQC
677 spectra were collected for each incremental addition of the unlabeled ligand (either
678 aptamer RNA, oleic acid, or elaidic acid) to the ^{15}N MSI1 sample to determine amide
679 proton chemical shift changes upon titration of the ligand. All experiments were
680 performed at 600 MHz on a Varian Inova spectrometer equipped with a triple-resonance
681 cold probe at 298 K. Data processing was performed using NMRPipe (Delaglio et al.
682 1995) and sparky (Goddard and Kneller) software.
683
684 **Molecular dynamics simulation**
685 We performed molecular dynamics (MD) simulations of the RRM1 domain of MSI1
686 (residues 20-96) free and bound to oleic acid. We modeled the unknown structure of
687 MSI1 bound to oleic acid by starting from the NMR solution structure of MSI1 RRM1
688 (Miyanoiri et al. 2003; Ohyama et al. 2011) and docking the oleic acid ligand using the
689 GLIDE software package from Schrödinger, LLC (Friesner et al. 2006), followed by

690 energy minimization and equilibration. All structures were solvated and neutralized in a
691 TIP3P water box (Jorgensen et al. 1986). Energy minimization and MD simulations were
692 subsequently carried out using the NAMD software package (Phillips et al. 2005) and
693 using the version 27 CHARMM potential energy function (MacKerell et al. 1998). The
694 particle mesh Ewald method (Darden et al. 1993; Essmann et al. 1995) was used to treat
695 electrostatic interactions and periodic boundary conditions were applied throughout. The
696 SHAKE algorithm (Ryckaert et al. 1977) was applied throughout the simulation to
697 constrain the hydrogen atom bond lengths at their equilibrium values and an integration
698 time step of 2 fs was used. After an initial energy minimization, the system was simulated
699 in the isothermal-isobaric ensemble. Non-bonded interactions were calculated every time
700 step using a cut-off distance of 12 Å. After equilibration in the isothermal-isobaric
701 ensemble, an additional stage of equilibration was performed in the microcanonical
702 ensemble. We then collected three independent 30 ns constant-NVE production runs of
703 MSI-1 bound to oleic acid and one for MSI-1 in the free state at an average temperature
704 of 298 K.
705 Visualization and secondary structure analysis was performed in VMD, using the
706 STRIDE method (Frishman and Argos 1995).
707 In addition, we employed a number of measures to characterize the structural and
708 dynamical changes between the free and bound state of MSI-1, including the radius of
709 gyration, the solvent accessible surface area (SASA), distance between backbone and/or
710 side chain atoms of residues G35-L85 and W29-Q30, and Lipari and Szabo order
711 parameters (Lipari and Szabo 1982; Humphrey et al. 1996). These quantities were

712 calculated using VMD (Humphrey et al. 1996) software along with bespoke programs
713 previously described elsewhere (Morgan and Massi 2010).
714
715 **Circular dichroism**
716 Far-UV circular dichroism (CD) spectra were collected using 10μM MSI1 in 50mM Tris
717 pH 8.0, 100mM NaCl and 0.1% TFE on a Jasco-810 spectropolarimeter (Jasco Inc.,
718 Easton, MD). Spectra were collected from 215-260 nm in a 0.2 cm path length quartz
719 cuvette using a scan rate of 20 nm min^{-1} and a response time of 8 s. The sample
720 temperature for all CD measurements was maintained at 293 K.
721
722 **Analytical ultracentrifugation**
723 Sedimentation velocity analyses were conducted using a Beckman Optima XL-I
724 analytical ultracentrifuge in the University of Massachusetts Medical School
725 Ultracentrifuge Facility. Data were analyzed with UltraScan III version 1.0 (Demeler et
726 al. 2011). Sedimentation velocity experiments were performed with 45 μM MSI1 in
727 storage buffer (50 mM Tris-HCl pH 8.0, 20 mM NaCl, 2 mM DTT). Measurements were
728 made at 20°C using an AN60ti rotor at 20000 rpm and 280 nm in intensity mode. Partial
729 specific volumes were estimated on the basis of peptide sequence with UltraScan and
730 found to be 0.7280 cm3/g for the MSI1 RBD. Data were analyzed by two-dimensional
731 spectrum analysis with simultaneous removal of time and radially invariant noise
732 (Demeler et al. 2009; Brookes et al. 2010). Noise and diffusion-corrected, model-
733 independent sedimentation coefficient distributions were generated using the enhanced
734 van Holde-Weischet analysis (Demeler et al. 1997; Demeler and van Holde 2004).

735

736 **Cell-based experiments**

737 **Cell lines and culture**

738 CG-4 rat oligodendrocyte progenitor and B104 neuroblastoma cells were a gift from
739 Lynn Hudson and were cultured as previously described (Louis et al. 1992). CG-4 cells
740 were maintained in the progenitor state in 30% B104 conditioned media. HEK293T cells
741 were cultured in Dulbecco's modified Eagle's medium (Invitrogen) with 10% fetal
742 bovine serum (Atlanta Biologicals Inc., Lawrenceville, GA), 100 units/ml penicillin, and
743 100 µg/ml streptomycin (Invitrogen).

744

745 **Proliferation assays**

746 100,000 HEK293T or CG-4 cells were seeded into each well of 6-well culture plates. 24
747 h after seeding, cells were treated with either 50 µM oleic acid in EtOH or EtOH only as
748 a control. 24, 48, and 72 h after fatty acid treatment, cells were assayed for proliferative
749 changes using the Cyquant direct cell proliferation assay (Invitrogen) according to the
750 manufacturers instructions using a Victor V3 plate reader (PerkinElmer). The treatment
751 concentration was chosen after a dose response for toxicity and efficacy across a range
752 defined by established protocols for neuroblastoma cells (Figure 7-figure 7 supplement 1)
753 (Di Loreto et al. 2007).

754

755 **RNA co-immunoprecipitation**

756 For each experiment, 10^6 CG-4 cells were crosslinked for 10 minutes with 0.1%
757 formaldehyde in PBS then scraped into lysis buffer (1% (w/v) SDS, 10 mM EDTA, 1x

EDTA-free protease inhibitors). Lysate was diluted in 10X IP buffer (0.01% SDS, 1.1% Triton X-100, 1.2mM EDTA, 16.7mM Tris-HCl, pH 8.1, 167mM NaCl) with 8 units SUPERase-In (Ambion). Immunoprecipitation was performed using rabbit polyclonal anti-Musashi 1 (Abcam ab21628) or rabbit polyclonal anti-GFAP (Abcam ab7260) conjugated to Dynabeads protein G (Invitrogen) according to the manufacturer's instructions. After proteinase K digestion (NEB) and heat-induced crosslink reversal, RNA was phenol-chloroform extracted, ethanol precipitated and resuspended in 20 µL nuclease-free water. RNA was then treated with DNase (Ambion Turbo DNAfree) to remove any DNA contamination. RNA was reverse transcribed and amplified using a SuperScript® III One-Step RT-PCR System with Platinum®Taq (Invitrogen) and transcript-specific fluorescein-labeled primers for *scd1* and *numb*. PCR products were separated from free primers on a 5% native polyacrylamide gel, imaged on a Fuji FLA-5000 imager, and quantified using Image Gauge software.

MSI1 overexpression and qRT-PCR

Twenty four hours prior to transfection, 10^6 HEK293T cells were seeded in 10 cm culture plates. Cells were transfected with 2 µg pCDH-CMV-MSI1(FL) or empty pCDH-CMV-MCS-EF1-Puro using Effectine reagent according the manufacturers instructions (Qiagen). 24 h after transfection, transfected cells were selected for with 2 µg/mL puromycin (Sigma). RNA and protein was harvested 72 h after transfection. To confirm MSI1 overexpression, RNA was collected using Trizol reagent (Invitrogen) followed by DNAse treatment (Turbo DNAfree, Ambion) according to the provided instructions. RNA yield was determined by spectrophotometry and quantitative RT-PCR was

781 performed with an Opticon thermal cycler (Bio-Rad) using an iScript One-Step RT-PCR
782 Kit with SYBR Green (Bio-Rad) according to the manufacturer's instructions. All assays
783 were performed in triplicate. Data were analyzed by sigmoidal curve fitting according to
784 the method of Rutledge (Rutledge 2004) and normalized to GTF2i or Tubulin.
785
786 **SCD western blots**
787 Cells were lysed with SDS lysis buffer (1% SDS, 10 mM EDTA, 1x EDTA-free protease
788 inhibitors) and protein concentration was determined by the bicinchoninic acid assay
789 method (BCA, Pierce) according to the manufacturer protocol. Samples were boiled for 5
790 minutes after the addition of 6x Laemmli buffer (9% SDS and 60% glycerol, 375 mM
791 Tris-HCl pH 6.8, 0.015% Bromophenol blue, 12% β-mercaptoethanol). Proteins were
792 separated for 2 h on a 12% SDS-polyacrylamide gel using a Bio-Rad mini-PROTEAN
793 electrophoresis apparatus, transferred to low-fluorescence PVDF membranes (Millipore)
794 for 2 h at 4ºC at a constant 70 V in 25mM Tris, 150mM glycine, and 10% (v/v) methanol
795 transfer buffer, blocked with Odyssey Blocking Buffer (OBB, LI-COR Biosciences) for 1
796 h at room temperature, and probed with 1:1000 dilution of mouse monoclonal anti-SCD
797 antibody (Abcam ab19862) in OBB overnight at 4ºC. After washing with PBS-T,
798 membranes were incubated with fluorescent goat anti-mouse secondary antibodies (LI-
799 COR Biosciences, 926-32210) at 1:15000 in OBB for 1 h at room temperature. Signal
800 was detected using an Odyssey Infrared Imaging System (LI-COR Biosciences). To
801 ensure antibody specificity, shRNA knockdown of SCD1 was performed with two
802 independent shRNA constructs (Open Biosystems V3LHS_305870 and V3LHS_305872)
803 and compared with non-silencing shRNA construct (Open Biosystems RHS4346).

804

805 **Total lipid extraction**

806 Cells were removed from plates with 0.25% Trypsin-EDTA (Gibco) and the total cell
807 number was obtained using a hemocytometer. Each sample contained 1-2x10^6 cells. After
808 pelleting by centrifugation, cells were resuspended in 200 µL H_20, immediately followed
809 by 250 µL methanol and 125 µL chloroform/0.01% Butylated hydroxytoluene (BHT).
810 Samples were shaken vigorously for 30 seconds, then an additional 250 µL
811 chloroform/0.01% BHT and 250 µL H_20 was added. After 30 seconds of additional
812 shaking, samples were centrifuged for 5 minutes at 4º C. The chloroform layer was
813 removed to a new tube, and the cell sample was treated with 250 µL of chloroform/0.01%
814 BHT, vigorous shaking, centrifuging and subsequent chloroform layer removal twice
815 more. Combined chloroform layers were washed with 500 µL KCL, then 500 µL H_2O.
816 Insoluble layers were transferred to glass vials and dried under argon. Samples were sent
817 to the Kansas lipidomics research center for analysis by mass spectrometry as previously
818 described (Welti et al. 2002). 5 independent biological replicates were analyzed for each
819 treatment group.

820

821 **Lipidomics data analysis**

822 The lipid profile data were acquired at Kansas Lipidomics Research Center (KLRC).
823 Instrument acquisition and method development at KLRC was supported by NSF grants
824 MCB 0455318, MCB 0920663, DBI 0521587, DBI 1228622, Kansas INBRE (NIH Grant
825 P20 RR16475 from the INBRE program of the National Center for Research Resources),
826 NSF EPSCoR grant EPS-0236913, Kansas Technology Enterprise Corporation, and

827 Kansas State University. Lipidomics data were reported as nMoles / $1x10^6$ cells. After
828 removing data points for samples with values below the limit of detection for the
829 instrumentation (0.02 nMoles / $1x10^6$ cells), all data points for which no signal was
830 detected in either treatment group were removed. A pseudocount of 0.002 nMoles / $1x10^6$
831 cells was added to all remaining data points. Outliers were eliminated using a Q test.
832 Significant differences between treatments for each lipid class were determined using a
833 Student's t-test and an FDR of 0.05.
834
835 **Critical micelle concentration determination**
836 The critical micelle concentration (CMC) for oleic acid in equilibration buffer was
837 determined using N-phenyl-1-naphthylamine (NPN), a compound that fluoresces when
838 sequestered into micelles (Hagihara et al. 2002; Hasegawa et al. 2008). 25 μM NPN was
839 incubated with varying amounts of oleic acid for 30 minutes. Fluorescence intensity was
840 determined with a Victor V3 plate reader using a 355 nm excitation filter and a 460 nm
841 emission filter. Fluorescence intensity data were plotted as a function of fatty acid
842 concentration. The CMC was determined by a two state segmented linear regression to
843 identify the breakpoint between baseline fluorescence and fluorescence caused by NPN
844 association with micelles.
845
846 **Acknowledgements**
847 The authors thank Dr. Ruth Zearfoss, Dr. Kendall Knight, and Dr. Phillip Zamore for
848 helpful discussions, Dr. Hong Cao for technical assistance with the small molecule
849 screen, Dr. Jill Zitzewitz for helpful discussions and advice concerning CD

measurements, Dr. Osman Bilsel and Sagar Kathuria for technical support and advice with intrinsic tryptophan fluorescence measurements, Sarah Swygert, Kim Crowly, Jeremy Mann, and Dr. Borries Demeler for help and advice with velocity sedimentation experiments, Alicia Bicknell and Dr. Melissa Moore for help and sharing equipment and reagents for IR western blot experiments, Dr. C. Robert Matthews for advice and sharing equipment, and the team at the Kansas lipidomics research center for quantitative lipidomics analysis and advice on preparing samples. This work was supported by NIH Grant GM098763 to F.M. and NIH Grants GM081422 and GM098643 to S.P.R.

References

Antson AA, Otridge J, Brzozowski AM, Dodson EJ, Dodson GG, Wilson KS, Smith TM, Yang M, Kurecki T, Gollnick P. 1995. The structure of trp RNA-binding attenuation protein. *Nature* **374**: 693-700.

Attie AD, Krauss RM, Gray-Keller MP, Brownlie A, Miyazaki M, Kastelein JJ, Lusis AJ, Stalenhoef AF, Stoehr JP, Hayden MR et al. 2002. Relationship between stearoyl-CoA desaturase activity and plasma triglycerides in human and mouse hypertriglyceridemia. *J Lipid Res* **43**: 1899-1907.

Babitzke P, Bear DG, Yanofsky C. 1995. TRAP, the trp RNA-binding attenuation protein of Bacillus subtilis, is a toroid-shaped molecule that binds transcripts containing GAG or UAG repeats separated by two nucleotides. *Proc Natl Acad Sci U S A* **92**: 7916-7920.

872 Battelli C, Nikopoulos GN, Mitchell JG, Verdi JM. 2006. The RNA-binding protein
873 Musashi-1 regulates neural development through the translational repression of
874 p21WAF-1. *Mol Cell Neurosci* **31**: 85-96.
875 Beiraghi S, Zhou M, Talmadge CB, Went-Sumegi N, Davis JR, Huang D, Saal H,
876 Seemayer TA, Sumegi J. 2003. Identification and characterization of a novel gene
877 disrupted by a pericentric inversion inv(4)(p13.1q21.1) in a family with cleft lip.
878 *Gene* **309**: 11-21.
879 Berger J, Moller DE. 2002. The mechanisms of action of PPARs. *Annu Rev Med* **53**: 409-
880 435.
881 Bocos C, Gottlicher M, Gearing K, Banner C, Enmark E, Teboul M, Crickmore A,
882 Gustafsson JA. 1995. Fatty acid activation of peroxisome proliferator-activated
883 receptor (PPAR). *J Steroid Biochem Mol Biol* **53**: 467-473.
884 Boland LM, Drzewiecki MM. 2008. Polyunsaturated fatty acid modulation of voltage-
885 gated ion channels. *Cell Biochem Biophys* **52**: 59-84.
886 Bradley RL, Fisher FF, Maratos-Flier E. 2008. Dietary fatty acids differentially regulate
887 production of TNF-alpha and IL-10 by murine 3T3-L1 adipocytes. *Obesity (Silver*
888 *Spring)* **16**: 938-944.
889 Brookes E, Demeler B, Rosano C, Rocco M. 2010. The implementation of SOMO
890 (SOlution MOdeller) in the UltraScan analytical ultracentrifugation data analysis
891 suite: enhanced capabilities allow the reliable hydrodynamic modeling of virtually
892 any kind of biomacromolecule. *European Biophysics Journal* **39**: 423-435.

893 Capaldi S, Guariento M, Perduca M, Di Pietro SM, Santome JA, Monaco HL. 2006.
894 Crystal structure of axolotl (Ambystoma mexicanum) liver bile acid-binding
895 protein bound to cholic and oleic acid. *Proteins* **64**: 79-88.
896 Castello A, Fischer B, Eichelbaum K, Horos R, Beckmann BM, Strein C, Davey NE,
897 Humphreys DT, Preiss T, Steinmetz LM et al. 2012. Insights into RNA biology
898 from an atlas of mammalian mRNA-binding proteins. *Cell* **149**: 1393-1406.
899 Charlesworth A, Wilczynska A, Thampi P, Cox LL, MacNicol AM. 2006. Musashi
900 regulates the temporal order of mRNA translation during Xenopus oocyte
901 maturation. *EMBO J* **25**: 2792-2801.
902 Chu E, Koeller DM, Casey JL, Drake JC, Chabner BA, Elwood PC, Zinn S, Allegra CJ.
903 1991. Autoregulation of human thymidylate synthase messenger RNA translation
904 by thymidylate synthase. *Proc Natl Acad Sci U S A* **88**: 8977-8981.
905 Chu E, Takimoto CH, Voeller D, Grem JL, Allegra CJ. 1993. Specific binding of human
906 dihydrofolate reductase protein to dihydrofolate reductase messenger RNA in
907 vitro. *Biochemistry* **32**: 4756-4760.
908 Ciesla J. 2006. Metabolic enzymes that bind RNA: yet another level of cellular regulatory
909 network? *Acta Biochim Pol* **53**: 11-32.
910 Clery A, Blatter M, Allain FH. 2008. RNA recognition motifs: boring? Not quite. *Curr*
911 *Opin Struct Biol* **18**: 290-298.
912 Coleman RA, Lee DP. 2004. Enzymes of triacylglycerol synthesis and their regulation.
913 *Prog Lipid Res* **43**: 134-176.
914 Darden T, York D, Pedersen L. 1993. Particle mesh Ewald: An N,ãÖlog(N) method for
915 Ewald sums in large systems. *The Journal of Chemical Physics* **98**: 10089-10092.

De Nuccio C, Bernardo A, De Simone R, Mancuso E, Magnaghi V, Visentin S, Minghetti L. 2011. Peroxisome proliferator-activated receptor gamma agonists accelerate oligodendrocyte maturation and influence mitochondrial functions and oscillatory Ca(2+) waves. *J Neuropathol Exp Neurol* **70**: 900-912.

de Sousa Abreu R, Sanchez-Diaz PC, Vogel C, Burns SC, Ko D, Burton TL, Vo DT, Chennasamudaram S, Le SY, Shapiro BA et al. 2009. Genomic analyses of musashi1 downstream targets show a strong association with cancer-related processes. *J Biol Chem* **284**: 12125-12135.

Delaglio F, Grzesiek S, Vuister GW, Zhu G, Pfeifer J, Bax A. 1995. NMRPipe: a multidimensional spectral processing system based on UNIX pipes. *Journal of biomolecular NMR* **6**: 277-293.

Demeler B, Brookes E, Wang R, Schirf V, Kim CA. 2009. Characterization of reversible associations by sedimentation velocity with UltraScan. *Macromolecular bioscience* **10**: 775-782.

Demeler B, Gorbet G, Zollars D, Brookes E, Cao W, Dubbs B. 2011. UltraScan III: UltraScan-III, a comprehensive analysis software for analytical ultracentrifugation experiments. The University of Texas Health Science Center at San Antonio, Dept. of Biochemistry.

Demeler B, Saber H, Hansen JC. 1997. Identification and interpretation of complexity in sedimentation velocity boundaries. *Biophysical journal* **72**: 397-407.

Demeler B, van Holde KE. 2004. Sedimentation velocity analysis of highly heterogeneous systems. *Anal Biochem* **335**: 279-288.

938 Di Loreto S, D'Angelo B, D'Amico MA, Benedetti E, Cristiano L, Cinque B, Cifone MG,
939 Ceru MP, Festuccia C, Cimini A. 2007. PPARbeta agonists trigger neuronal
940 differentiation in the human neuroblastoma cell line SH-SY5Y. *Journal of*
941 *cellular physiology* **211**: 837-847.
942 Dobson NR, Zhou YX, Flint NC, Armstrong RC. 2008. Musashi1 RNA-binding protein
943 regulates oligodendrocyte lineage cell differentiation and survival. *Glia* **56**: 318-
944 330.
945 Dollenmaier G, Weitz M. 2003. Interaction of glyceraldehyde-3-phosphate
946 dehydrogenase with secondary and tertiary RNA structural elements of the
947 hepatitis A virus 3' translated and non-translated regions. *J Gen Virol* **84**: 403-
948 414.
949 Essmann U, Perera L, Berkowitz M, Darden T, Lee H, Pedersen L. 1995. A smooth
950 particle mesh Ewald method. *The Journal of Chemical Physics* **103**: 8577-8593.
951 Farley BM, Pagano JM, Ryder SP. 2008. RNA target specificity of the embryonic cell
952 fate determinant POS-1. *RNA* **14**: 2685-2697.
953 Forman BM, Chen J, Evans RM. 1997. Hypolipidemic drugs, polyunsaturated fatty acids,
954 and eicosanoids are ligands for peroxisome proliferator-activated receptors alpha
955 and delta. *Proc Natl Acad Sci U S A* **94**: 4312-4317.
956 Franklin RJ, Bayley SA, Milner R, Ffrench-Constant C, Blakemore WF. 1995.
957 Differentiation of the O-2A progenitor cell line CG-4 into oligodendrocytes and
958 astrocytes following transplantation into glia-deficient areas of CNS white matter.
959 *Glia* **13**: 39-44.

960 Friesner RA, Banks JL, Murphy RB, Halgren TA, Klicic JJ, Mainz DT, Repasky MP,
961 Knoll EH, Shelley M, Perry JK et al. 2004. Glide: a new approach for rapid,
962 accurate docking and scoring. 1. Method and assessment of docking accuracy. *J*
963 *Med Chem* **47**: 1739-1749.
964 Friesner RA, Murphy RB, Repasky MP, Frye LL, Greenwood JR, Halgren TA,
965 Sanschagrin PC, Mainz DT. 2006. Extra precision glide: docking and scoring
966 incorporating a model of hydrophobic enclosure for protein-ligand complexes. *J*
967 *Med Chem* **49**: 6177-6196.
968 Frishman D, Argos P. 1995. Knowledge,Äêbased protein secondary structure
969 assignment. *Proteins: Structure, Function, and Bioinformatics* **23**: 566-579.
970 Gollnick P, Ishino S, Kuroda MI, Henner DJ, Yanofsky C. 1990. The mtr locus is a two-
971 gene operon required for transcription attenuation in the trp operon of Bacillus
972 subtilis. *Proc Natl Acad Sci U S A* **87**: 8726-8730.
973 Gottlicher M, Widmark E, Li Q, Gustafsson JA. 1992. Fatty acids activate a chimera of
974 the clofibric acid-activated receptor and the glucocorticoid receptor. *Proc Natl*
975 *Acad Sci U S A* **89**: 4653-4657.
976 Griffiths I, Klugmann M, Anderson T, Yool D, Thomson C, Schwab MH, Schneider A,
977 Zimmermann F, McCulloch M, Nadon N et al. 1998. Axonal swellings and
978 degeneration in mice lacking the major proteolipid of myelin. *Science* **280**: 1610-
979 1613.
980 Grundy FJ, Lehman SC, Henkin TM. 2003. The L box regulon: lysine sensing by leader
981 RNAs of bacterial lysine biosynthesis genes. *Proc Natl Acad Sci U S A* **100**:
982 12057-12062.

983 Gurvitz A, Rottensteiner H. 2006. The biochemistry of oleate induction: transcriptional
984 upregulation and peroxisome proliferation. *Biochim Biophys Acta* **1763**: 1392-
985 1402.
986 Hagihara Y, Hong DP, Hoshino M, Enjyoji K, Kato H, Goto Y. 2002. Aggregation of
987 beta(2)-glycoprotein I induced by sodium lauryl sulfate and lysophospholipids.
988 *Biochemistry* **41**: 1020-1026.
989 Halgren TA, Murphy RB, Friesner RA, Beard HS, Frye LL, Pollard WT, Banks JL. 2004.
990 Glide: a new approach for rapid, accurate docking and scoring. 2. Enrichment
991 factors in database screening. *J Med Chem* **47**: 1750-1759.
992 Hasegawa K, Tsutsumi-Yasuhara S, Ookoshi T, Ohhashi Y, Kimura H, Takahashi N,
993 Yoshida H, Miyazaki R, Goto Y, Naiki H. 2008. Growth of beta(2)-
994 microglobulin-related amyloid fibrils by non-esterified fatty acids at a neutral pH.
995 *Biochem J* **416**: 307-315.
996 Hemmati HD, Nakano I, Lazareff JA, Masterman-Smith M, Geschwind DH, Bronner-
997 Fraser M, Kornblum HI. 2003. Cancerous stem cells can arise from pediatric
998 brain tumors. *Proc Natl Acad Sci U S A* **100**: 15178-15183.
999 Hentze MW, Argos P. 1991. Homology between IRE-BP, a regulatory RNA-binding
1000 protein, aconitase, and isopropylmalate isomerase. *Nucleic Acids Res* **19**: 1739-
1001 1740.
1002 Hentze MW, Preiss T. 2010. The REM phase of gene regulation. *Trends Biochem Sci* **35**:
1003 423-426.
1004 Humphrey W, Dalke A, Schulten K. 1996. VMD: visual molecular dynamics. *Journal of*
1005 *molecular graphics* **14**: 33-38.

1006 Imai T, Tokunaga A, Yoshida T, Hashimoto M, Mikoshiba K, Weinmaster G, Nakafuku
1007 M, Okano H. 2001. The neural RNA-binding protein Musashi1 translationally
1008 regulates mammalian numb gene expression by interacting with its mRNA. *Mol*
1009 *Cell Biol* **21**: 3888-3900.
1010 Ito T, Kwon HY, Zimdahl B, Congdon KL, Blum J, Lento WE, Zhao C, Lagoo A,
1011 Gerrard G, Foroni L et al. 2010. Regulation of myeloid leukaemia by the cell-fate
1012 determinant Musashi. *Nature* **466**: 765-768.
1013 James MJ, Gibson RA, Cleland LG. 2000. Dietary polyunsaturated fatty acids and
1014 inflammatory mediator production. *Am J Clin Nutr* **71**: 343S-348S.
1015 Johnson M, Ekonomou A, Hobbs C, Ballard CG, Perry RH, Perry EK. 2010. Neurogenic
1016 marker abnormalities in the hippocampus in dementia with Lewy bodies.
1017 *Hippocampus*.
1018 Jorgensen WL, Chandrasekhar J, Buckner JK, Madura JD. 1986. Computer simulations
1019 of organic reactions in solution. *Ann N Y Acad Sci* **482**: 198-209.
1020 Kaneko Y, Sakakibara S, Imai T, Suzuki A, Nakamura Y, Sawamoto K, Ogawa Y,
1021 Toyama Y, Miyata T, Okano H. 2000. Musashi1: an evolutionally conserved
1022 marker for CNS progenitor cells including neural stem cells. *Dev Neurosci* **22**:
1023 139-153.
1024 Kharas MG, Lengner CJ, Al-Shahrour F, Bullinger L, Ball B, Zaidi S, Morgan K, Tam
1025 W, Paktinat M, Okabe R et al. 2010. Musashi-2 regulates normal hematopoiesis
1026 and promotes aggressive myeloid leukemia. *Nat Med* **16**: 903-908.
1027 Kielkopf CL, Lucke S, Green MR. 2004. U2AF homology motifs: protein recognition in
1028 the RRM world. *Genes Dev* **18**: 1513-1526.

1029 Kliewer SA, Sundseth SS, Jones SA, Brown PJ, Wisely GB, Koble CS, Devchand P,
1030 Wahli W, Willson TM, Lenhard JM et al. 1997. Fatty acids and eicosanoids
1031 regulate gene expression through direct interactions with peroxisome proliferator-
1032 activated receptors alpha and gamma. *Proc Natl Acad Sci U S A* **94**: 4318-4323.
1033 Kubodera T, Watanabe M, Yoshiuchi K, Yamashita N, Nishimura A, Nakai S, Gomi K,
1034 Hanamoto H. 2003. Thiamine-regulated gene expression of Aspergillus oryzae
1035 thiA requires splicing of the intron containing a riboswitch-like domain in the 5'-
1036 UTR. *FEBS Lett* **555**: 516-520.
1037 Lam TT, Fu J, Hrynewycz M, Tso MO. 1995. The effect of aurintricarboxylic acid, an
1038 endonuclease inhibitor, on ischemia/reperfusion damage in rat retina. *J Ocul*
1039 *Pharmacol Ther* **11**: 253-259.
1040 Li J, Ding SF, Habib NA, Fermor BF, Wood CB, Gilmour RS. 1994. Partial
1041 characterization of a cDNA for human stearoyl-CoA desaturase and changes in its
1042 mRNA expression in some normal and malignant tissues. *Int J Cancer* **57**: 348-
1043 352.
1044 Lin SY, Riggs AD. 1972. Lac repressor binding to non-operator DNA: detailed studies
1045 and a comparison of eequilibrium and rate competition methods. *J Mol Biol* **72**:
1046 671-690.
1047 Lipari G, Szabo A. 1982. Model-free approach to the interpretation of nuclear magnetic
1048 resonance relaxation in macromolecules. 1. Theory and range of validity. *Journal*
1049 *of the American Chemical Society* **104**: 4546-4559.
1050 Liu X, Strable MS, Ntambi JM. 2011. Stearoyl CoA desaturase 1: role in cellular
1051 inflammation and stress. *Adv Nutr* **2**: 15-22.

1052 Louis JC, Magal E, Muir D, Manthorpe M, Varon S. 1992. CG-4, a new bipotential glial
1053 cell line from rat brain, is capable of differentiating in vitro into either mature
1054 oligodendrocytes or type-2 astrocytes. *J Neurosci Res* **31**: 193-204.
1055 MacKerell AD, Bashford D, Bellott, Dunbrack RL, Evanseck JD, Field MJ, Fischer S,
1056 Gao J, Guo H, Ha S et al. 1998. All-Atom Empirical Potential for Molecular
1057 Modeling and Dynamics Studies of Proteins,Ä†. *The Journal of Physical*
1058 *Chemistry B* **102**: 3586-3616.
1059 Mandal M, Boese B, Barrick JE, Winkler WC, Breaker RR. 2003. Riboswitches control
1060 fundamental biochemical pathways in Bacillus subtilis and other bacteria. *Cell*
1061 **113**: 577-586.
1062 Mandal M, Breaker RR. 2004. Adenine riboswitches and gene activation by disruption of
1063 a transcription terminator. *Nat Struct Mol Biol* **11**: 29-35.
1064 Mandal M, Lee M, Barrick JE, Weinberg Z, Emilsson GM, Ruzzo WL, Breaker RR.
1065 2004. A glycine-dependent riboswitch that uses cooperative binding to control
1066 gene expression. *Science* **306**: 275-279.
1067 Martinez M, Mougan I. 1998. Fatty acid composition of human brain phospholipids
1068 during normal development. *J Neurochem* **71**: 2528-2533.
1069 Menendez JA, Papadimitropoulou A, Vellon L, Lupu R. 2006. A genomic explanation
1070 connecting "Mediterranean diet", olive oil and cancer: oleic acid, the main
1071 monounsaturated fatty acid of olive oil, induces formation of inhibitory "PEA3
1072 transcription factor-PEA3 DNA binding site" complexes at the Her-2/neu (erbB-
1073 2) oncogene promoter in breast, ovarian and stomach cancer cells. *Eur J Cancer*
1074 **42**: 2425-2432.

1075 Minville-Walz M, Pierre AS, Pichon L, Bellenger S, Fevre C, Bellenger J, Tessier C,
1076 Narce M, Rialland M. 2010. Inhibition of stearoyl-CoA desaturase 1 expression
1077 induces CHOP-dependent cell death in human cancer cells. *PLoS One* **5**: e14363.
1078 Miyanoiri Y, Kobayashi H, Imai T, Watanabe M, Nagata T, Uesugi S, Okano H, Katahira
1079 M. 2003. Origin of higher affinity to RNA of the N-terminal RNA-binding
1080 domain than that of the C-terminal one of a mouse neural protein, musashi1, as
1081 revealed by comparison of their structures, modes of interaction, surface
1082 electrostatic potentials, and backbone dynamics. *J Biol Chem* **278**: 41309-41315.
1083 Miyazaki M, Kim YC, Gray-Keller MP, Attie AD, Ntambi JM. 2000. The biosynthesis of
1084 hepatic cholesterol esters and triglycerides is impaired in mice with a disruption
1085 of the gene for stearoyl-CoA desaturase 1. *J Biol Chem* **275**: 30132-30138.
1086 Morgan BR, Massi F. 2010. A computational study of RNA binding and specificity in the
1087 tandem zinc finger domain of TIS11d. *Protein Sci* **19**: 1222-1234.
1088 Nagata T, Kanno R, Kurihara Y, Uesugi S, Imai T, Sakakibara S, Okano H, Katahira M.
1089 1999. Structure, backbone dynamics and interactions with RNA of the C-terminal
1090 RNA-binding domain of a mouse neural RNA-binding protein, Musashi1. *J Mol*
1091 *Biol* **287**: 315-330.
1092 Nguyen MT, Favelyukis S, Nguyen AK, Reichart D, Scott PA, Jenn A, Liu-Bryan R,
1093 Glass CK, Neels JG, Olefsky JM. 2007. A subpopulation of macrophages
1094 infiltrates hypertrophic adipose tissue and is activated by free fatty acids via Toll-
1095 like receptors 2 and 4 and JNK-dependent pathways. *J Biol Chem* **282**: 35279-
1096 35292.

1097 Ohyama T, Nagata T, Tsuda K, Kobayashi N, Imai T, Okano H, Yamazaki T, Katahira
1098 M. 2011. Structure of Musashi1 in a complex with target RNA: the role of
1099 aromatic stacking interactions. *Nucleic Acids Res* **40**: 3218-3231.
1100 Pagano JM, Clingman CC, Ryder SP. 2011. Quantitative approaches to monitor protein-
1101 nucleic acid interactions using fluorescent probes. *RNA* **17**: 14-20.
1102 Pagano JM, Farley BM, McCoig LM, Ryder SP. 2007. Molecular basis of RNA
1103 recognition by the embryonic polarity determinant MEX-5. *J Biol Chem* **282**:
1104 8883-8894.
1105 Phillips JC, Braun R, Wang W, Gumbart J, Tajkhorshid E, Villa E, Chipot C, Skeel RD,
1106 Kale L, Schulten K. 2005. Scalable molecular dynamics with NAMD. *J Comput*
1107 *Chem* **26**: 1781-1802.
1108 Preiss T, Hall AG, Lightowlers RN. 1993. Identification of bovine glutamate
1109 dehydrogenase as an RNA-binding protein. *J Biol Chem* **268**: 24523-24526.
1110 Reines SA, Cantor CR. 1974. New fluorescent hydrazide reagents for the oxidized 3'-
1111 terminus of RNA. *Nucleic Acids Res* **1**: 767-786.
1112 Rios-Esteves J, Resh MD. 2013. Stearoyl CoA desaturase is required to produce active,
1113 lipid-modified Wnt proteins. *Cell Rep* **4**: 1072-1081.
1114 Roth A, Breaker RR. 2009. The structural and functional diversity of metabolite-binding
1115 riboswitches. *Annu Rev Biochem* **78**: 305-334.
1116 Rouault TA, Stout CD, Kaptain S, Harford JB, Klausner RD. 1991. Structural
1117 relationship between an iron-regulated RNA-binding protein (IRE-BP) and
1118 aconitase: functional implications. *Cell* **64**: 881-883.

1119 Rutledge RG. 2004. Sigmoidal curve-fitting redefines quantitative real-time PCR with the
1120 prospective of developing automated high-throughput applications. *Nucleic Acids*
1121 *Res* **32**: e178.
1122 Ryazanov AG. 1985. Glyceraldehyde-3-phosphate dehydrogenase is one of the three
1123 major RNA-binding proteins of rabbit reticulocytes. *FEBS Lett* **192**: 131-134.
1124 Ryckaert J-P, Ciccotti G, Berendsen HJ. 1977. Numerical integration of the cartesian
1125 equations of motion of a system with constraints: molecular dynamics of< i>
1126 n</i>-alkanes. *Journal of Computational Physics* **23**: 327-341.
1127 Ryder SP, Williamson JR. 2004. Specificity of the STAR/GSG domain protein Qk1:
1128 implications for the regulation of myelination. *RNA* **10**: 1449-1458.
1129 Sakakibara S, Imai T, Hamaguchi K, Okabe M, Aruga J, Nakajima K, Yasutomi D,
1130 Nagata T, Kurihara Y, Uesugi S et al. 1996. Mouse-Musashi-1, a neural RNA-
1131 binding protein highly enriched in the mammalian CNS stem cell. *Dev Biol* **176**:
1132 230-242.
1133 Sakakibara S, Nakamura Y, Yoshida T, Shibata S, Koike M, Takano H, Ueda S,
1134 Uchiyama Y, Noda T, Okano H. 2002. RNA-binding protein Musashi family:
1135 roles for CNS stem cells and a subpopulation of ependymal cells revealed by
1136 targeted disruption and antisense ablation. *Proc Natl Acad Sci U S A* **99**: 15194-
1137 15199.
1138 Sanchez-Diaz PC, Burton TL, Burns SC, Hung JY, Penalva LO. 2008. Musashi1
1139 modulates cell proliferation genes in the medulloblastoma cell line Daoy. *BMC*
1140 *Cancer* **8**: 280.

1141 Scaglia N, Chisholm JW, Igal RA. 2009. Inhibition of stearoylCoA desaturase-1
1142 inactivates acetyl-CoA carboxylase and impairs proliferation in cancer cells: role
1143 of AMPK. *PLoS One* **4**: e6812.
1144 Scaglia N, Igal RA. 2008. Inhibition of Stearoyl-CoA Desaturase 1 expression in human
1145 lung adenocarcinoma cells impairs tumorigenesis. *Int J Oncol* **33**: 839-850.
1146 Shi H, Kokoeva MV, Inouye K, Tzameli I, Yin H, Flier JS. 2006. TLR4 links innate
1147 immunity and fatty acid-induced insulin resistance. *J Clin Invest* **116**: 3015-3025.
1148 Sudarsan N, Barrick JE, Breaker RR. 2003. Metabolite-binding RNA domains are present
1149 in the genes of eukaryotes. *RNA* **9**: 644-647.
1150 Sureban SM, May R, George RJ, Dieckgraefe BK, McLeod HL, Ramalingam S,
1151 Bishnupuri KS, Natarajan G, Anant S, Houchen CW. 2008. Knockdown of RNA
1152 binding protein musashi-1 leads to tumor regression in vivo. *Gastroenterology*
1153 **134**: 1448-1458.
1154 Swinnen JV, Vanderhoydonc F, Elgamal AA, Eelen M, Vercaeren I, Joniau S, Van
1155 Poppel H, Baert L, Goossens K, Heyns W et al. 2000. Selective activation of the
1156 fatty acid synthesis pathway in human prostate cancer. *Int J Cancer* **88**: 176-179.
1157 Toda M, Iizuka Y, Yu W, Imai T, Ikeda E, Yoshida K, Kawase T, Kawakami Y, Okano
1158 H, Uyemura K. 2001. Expression of the neural RNA-binding protein Musashi1 in
1159 human gliomas. *Glia* **34**: 1-7.
1160 Vitreschak AG, Rodionov DA, Mironov AA, Gelfand MS. 2003. Regulation of the
1161 vitamin B12 metabolism and transport in bacteria by a conserved RNA structural
1162 element. *RNA* **9**: 1084-1097.

1163 Vivian JT, Callis PR. 2001. Mechanisms of tryptophan fluorescence shifts in proteins.
1164 *Biophys J* **80**: 2093-2109.
1165 Wang X, Sato R, Brown MS, Hua X, Goldstein JL. 1994. SREBP-1, a membrane-bound
1166 transcription factor released by sterol-regulated proteolysis. *Cell* **77**: 53-62.
1167 Welti R, Li W, Li M, Sang Y, Biesiada H, Zhou HE, Rajashekar CB, Williams TD, Wang
1168 X. 2002. Profiling membrane lipids in plant stress responses. Role of
1169 phospholipase D alpha in freezing-induced lipid changes in Arabidopsis. *J Biol*
1170 *Chem* **277**: 31994-32002.
1171 Winkler WC, Breaker RR. 2003. Genetic control by metabolite-binding riboswitches.
1172 *Chembiochem* **4**: 1024-1032.
1173 -. 2005. Regulation of bacterial gene expression by riboswitches. *Annu Rev Microbiol* **59**:
1174 487-517.
1175 Yakhnin H, Zhang H, Yakhnin AV, Babitzke P. 2004. The trp RNA-binding attenuation
1176 protein of Bacillus subtilis regulates translation of the tryptophan transport gene
1177 trpP (yhaG) by blocking ribosome binding. *J Bacteriol* **186**: 278-286.
1178 Yokota N, Mainprize TG, Taylor MD, Kohata T, Loreto M, Ueda S, Dura W,
1179 Grajkowska W, Kuo JS, Rutka JT. 2004. Identification of differentially expressed
1180 and developmentally regulated genes in medulloblastoma using suppression
1181 subtraction hybridization. *Oncogene* **23**: 3444-3453.
1182 Zhang L, Ge L, Parimoo S, Stenn K, Prouty SM. 1999. Human stearoyl-CoA desaturase:
1183 alternative transcripts generated from a single gene by usage of tandem
1184 polyadenylation sites. *Biochem J* **340 (Pt 1)**: 255-264.
1185

1186

Legends

Figure 1: MSI1 is inhibited by monounsaturated fatty acids. (**A**) Pattern of MSI1 (blue) in the CNS. (**B-D**) EMSA and FP of MSI1 binding to RNA aptamer CCCR005 (AGCGUUAGUUAUUUAGUUCG). EMSA data (red line) were fit to the Hill equation where all shifted species were fit as an aggregate. FP data (black line) were fit to a two-site binding model. (**E-F**) Assay scheme for the inhibitor screen (**E**) and F-EMSA dose responses with hits identified from the small molecule screens (**E**) and oleic and elaidic acid (**F**). Each gel is one representative experiment of at least three independent experiments. No compound and no protein lanes identify the position of bound and free RNA migration, respectively.

Figure 2: Structure-activity relationship analysis demonstrates specificity of inhibition. **(A)** Small molecule screen hits. Compound ID (CID) refers to each compound's LOPAC identification number. Screen scores were calculated by normalizing the polarization value of each compound to the no protein and no compound controls, as described in the supplemental methods. After the screen was complete, compounds that scored as hits were confirmed by FP and F-EMSA dose response experiments. Apparent inhibition constants ($K_{i,\,app}$) are the average and standard deviation of at least three independent experiments. **(B)** The code = carbon number : number of double bonds, followed by the position of the double bonds from the aliphatic end of the fatty acid. Where a fatty acid is modified, the parental fatty acid numerical code is given in parentheses for comparison purposes. FP and F-EMSA dose response results are reported as the average and standard deviation of at least three independent experiments.

Figure 3: MSI1 inhibition is allosteric. **(A)** MSI1 tryptophan fluorescence at 350 nm as a function of oleic and elaidic acid. The $K_{d, app}$, $K_{i, app}$, and Hill parameters are the average and standard deviation of three independent replicates. (**B**) Ribbon model of MSI1 RRM1 (top). Space-filling model of MSI1 RRM1 (middle) and RRM2 (bottom) (Nagata et al. 1999; Miyanoiri et al. 2003). Left, β-sheet surface, right, α-helical surface. Conserved phenylalanines and W29 are green. Lysine and arginine residues are blue. A hydrophobic pocket exists on the RRM1 α-helical surface. (**C**) CD spectra of MSI1 RRM1 in the presence of oleic (top) or elaidic acid (bottom). (**D**) Envelope traces of the van Holde-Weischet analysis for analytical ultracentrifugation experiments of MSI1 alone (top), with oleic acid (middle) and with elaidic acid (bottom). The predominant species sediments where monomeric MSI1 would be expected, and there is no significant change in the sedimentation profile after addition of oleic or elaidic acid. Data are representative traces from one of three independent experiments.

Figure 4: (**A-B**) Model of RRM1 bound to oleic acid (yellow) calculated by Schrödinger GLIDE (Friesner et al. 2004; Friesner et al. 2006). (**C**) Overlay of the oleic acid bound MD simulation (gray and red) with the apo-state NMR structure (gray and blue) (Ohyama et al. 2011). (**D**) RNA contact residues (red) in loop 5, helix 2, and strand 4 of the β-sheet are perturbed in oleic acid-bound molecular dynamics simulation (Ohyama et al. 2011). **(E-F)** A representative snapshot from the MD simulation of MSI1 bound to oleic acid (white) compared to the MSI1-RNA NMR structure (blue) (Ohyama et al. 2011). Panel (**E**) shows the Gua 1 binding pocket. In the oleic-bound state, the open conformation of loop 5 (L5) orients K88 such that K88 cannot contact Gua 1. W29 is stacked against Q30

and unavailable for stacking against Gua 1. Interaction with the side chain of R61 stabilizes the conformation of W29 in the oleic-bound state. Panel (**F**) highlights the different conformations of residues that interact with Gua 1, Ura 2, Ade 3 and Gua 4; represented in grey, orange, red and purple, respectively. **(G)** Difference of the mean Lipari-Szabo order parameters by residue between the apo and oleic acid-bound states of MSI1. The Lipari-Szabo order parameters for the backbone NH bond vectors, S^2, were calculated to quantify the backbone flexibility of the free and oleic acid-bound form of MSI1. The difference of the order parameters, $\Delta S^2 = S^2_{apo} - S^2_{MSI\text{-}OA}$, indicates that MSI1-oleic acid complex is more flexible than apo MSI1, with the few exceptions mostly observed at the N-terminus. The secondary structural elements are highlighted at the top. Error bars are calculated from the standard deviation among trajectories.

Figure 5: Molecular dynamics studies (**A-B**) represent the normalized histograms of the protein solvent accessible surface area (SASA) and radius of gyration (r_{gyr}) illustrating the structural transition undergone by the MSI1 upon oleic acid binding. (**A**) SASA distributions calculated from the MD trajectories of MSI1 bound to oleic acid and of MSI1 in the apo state are represented in red and black, respectively. (**B**) Radius of gyration distributions calculated from the MD trajectories of MSI-1 bound to oleic acid and of MSI1 in the apo state are represented in red and black, respectively. (**C**) The probability of being in an α-helix or β-sheet is shown for each residue of MSI1. The probabilities calculated for each residue from the MD trajectories of MSI1 free and bound to oleic acid are shown in black and red, respectively. Oleic acid binding is associated with stabilization of the C-terminus of α-helix 1, fraying of α-helix 2, at both

1257 the N- and C-termini, extension of sheet 2, as well as the formation of an additional β-
1258 sheet at loop 5 (L5). (**D-E**) Normalized histograms of the distance between G35, located
1259 on α-helix 1, and L85, located on loop 5, calculated from the MD trajectories of oleic
1260 acid-bound MSI-1 and of apo MSI1 are shown in red and black, respectively. The
1261 distribution of distances between the C_α atoms of G35 and L85 is depicted in (**D**). The
1262 distribution of distances between the C_α of G35 and the $C_{\delta 2}$ of L85 is shown in (**E**). The
1263 green lines show the values of these distances observed in the NMR structure of MSI1
1264 bound to RNA (PDB ID 2RS2). In the oleic-bound state, loop 5 is restricted in
1265 approaching α-helix 1 due to the steric hindrance of the oleic acid. (**F-G**) Normalized
1266 histograms of two representative side chain distances of W29 and Q30. Histograms
1267 calculated over the MD trajectories of oleic acid-bound MSI1 are shown in red, those of
1268 apo MSI1 in black. The distance between W29 $C_{\varepsilon 2}$ and Q30 C_γ is shown in (**F**). The
1269 distance between W29 $C_{\zeta 2}$ and Q30 $N_{\varepsilon 2}$ is shown in (**G**). The green lines show these
1270 distances observed in the NMR structure of MSI1 bound to RNA (PDB ID 2RS2). In the
1271 oleic-bound state, the side chain of W29 is stacked against the side chain of Q30. This
1272 conformation of W29 is not observed in either the free or RNA-bound states of MSI1.
1273
1274 Figure 6: MSI-1 regulates stearoyl-CoA desaturase. (**A**) HEK293T (dashed) and CG-4
1275 (solid) cell proliferation as a function of oleic acid or stearic acid treatment (red = treated,
1276 black = untreated). The data is the average and standard deviation of at least three
1277 biological replicates. (**B**) There are seven MSI-1 consensus sites in the 3'-UTR of *Scd-1*
1278 mRNA. The $K_{d,\,app}$ is the average and standard deviation of at least three experiments. (**C**)
1279 *Scd-1* transcripts co-immunoprecipitate with anti-MSI-1 antibodies. The data were

quantified using a FUJI FLA-5000 imager. (**D**) Western analysis of SCD expression in HEK293T cells. The data were quantified using the LICOR Odyssey system relative to non specific bands (** and *, Figure 6-figure 6 supplement 2B) to control for loading. The average and standard deviation of at least three independent experiments is shown. (**E-H**) Lipidomics analysis of HEK293t cells ± MSI1 expression. Source data are included in Figure 6 source data 1. (**E**) Volcano plot of lipidomics data. Dashed lines denote fold-changes of ±1.5 and ±3. Red data points indicate lipids that are significantly changed upon MSI1 expression. (**F**) Scatter plot of lipidomics data. Data are reported as nMoles per million cells. Red data points indicate lipids that are significantly changed upon MSI1 expression (FDR = 0.05). (**G**) Fold-changes of the total cholesterol esters and two TAG classes in which 38 of the 54 significantly changing lipids are categorized. Each class changes significantly with MSI1 overexpression ($P < 0.05$). (**H**) Fold-changes for the four lipids that comprise the total cholesterol esters class. All display significant changes with MSI1 expression (FDR = 0.05).

Figure 7: Model of SCD regulation by MSI1, and subsequent downstream consequences of SCD activity changes.

Movie 1: This movie is a representative segment of an MD trajectory of MSI1 bound to oleic acid.

Figure 1 supplement 1: (**A**) Coomassie-stained SDS page gel shows that recombinant MSI1 is purified to greater than 95% over a 3-column purification protocol. (**B**) MSI1

displays decreased affinity for an RNA aptamer upon addition of oleic acid. Apparent dissociation constants were determined by plotting fluorescence polarization as a function of MSI1 protein concentration and fitting the data to the Hill equation. 0 μM oleic acid: $K_{d, app}$ = 16.3 ± 1.2 nM; 1 μM oleic acid: $K_{d, app}$ = 18.1 ± 2.6 nM; 10 μM oleic acid: $K_{d, app}$ = 40.5 ± 3.5 nM; 0 μM oleic acid: $K_{d, app}$ > 2000 nM. (**C**) CMC determination by N-phenyl-1-naphthylamine (NPN) fluorescence in equilibration buffer (pH 8.0). Segmented linear regression was used to determine the breakpoint between baseline and micelle-associated NPN fluorescence. The value of the CMC presented is the average and standard deviation from three experiments.

Figure 2 supplement 1: RNA binding specificity and inhibition by specific fatty acids is conserved in MSI2. (**A**) Sequence alignment shows 83% conservation between MSI1 and MSI2 within the RRM domains. Regions that correspond to α-helices, β-sheets, and intervening loops as defined by NMR spectroscopy are diagramed above the alignment. (**B**) MSI2 binds the MSI1 RNA aptamer CCCR005 with similar affinity to that of MSI1 by both FP and F-EMSA. The no protein control lane defines the position of free RNA. Data are the average and standard deviation of three independent experiments. (**C**) MSI2 is specifically inhibited by oleic acid and eicosenoic acid in FP and F-EMSA dose response experiments. No compound and no protein controls define the position of bound and free RNA respectively. Data are the average and standard deviation of three independent experiments.

Figure 3 supplement 1: (**A-D)** The MSI1 tryptophan fluorescence spectrum changes as a function of inhibitor titration. The tryptophan fluorescence emission spectrum is strongly quenched upon oleic acid (**A**) and erucic acid (**C**) but not elaidic acid (**B**) addition. (**D**) A tryptophan-containing control N-acetyl-tryptophanamide (NATA) does not change upon compound addition. Data from one representative experiment for each compound concentration are shown. (**E**) Difference spectra calculated for the far-UV CD spectra of MSI-1 collected at increasing oleic acid concentrations relative to the spectrum in the absence of oleic acid. Different colors correspond to different concentration of oleic acid: red is 3 μM, purple is 6 μM, blue is 12.5 μM, green is 25 μM and black is 50 μM. The inset shows the same difference spectra calculated for the CD spectra of MSI1 with increasing elaidic acid concentration relative to the spectrum collected in the absence of elaidic acid. The same color scheme applies to the different elaidic acid concentrations.

Figure 3 supplement 2: **(A-B)** Recombinant His6-tagged MSI1 RRM1 binds RNA aptamer CCCR005 (**A**) and is inhibited by oleic acid (**B**). FP data is reported as the average and standard deviation of three independent experiments. (**C**) 2D ^{1}H-^{15}N HSQC spectra of MSI1 free (red) and bound to RNA (blue) at pH 7 and 25 °C. Selected resonances are labeled and enlarged in the insets. Crosspeaks are colored according to the increasing concentration of added RNA. (**D-F**) NMR titration of oleic acid (**D**) The cross peak intensities (I) from the 2D ^{1}H-^{15}N HSQC spectra of MSI1 are plotted for four representative residues (Q30 black, R82 green, K98 red, A100 blue) as a function of the concentration of oleic acid added to sample of 133 μM MSI1 at pH 7 and 25 °C. The intensities are normalized relative to the measured intensity in the absence of oleic acid,

I_0. The intensity ratios were fitted to straight lines. (**E**) The cross peak intensities for all assigned residues of MSI1 in the 2D NMR spectrum after adding 0.22 molar equivalents of oleic acid. I_0 is the intensity without oleic acid addition and $I_{0.22}$ is the intensity after addition of 0.22 molar equivalents of oleic acid. Each point represents the $I_{0.22}/I_0$ for a single residue. The average of all intensities at $I_{0.22}$ (solid line) and ± 1 standard deviation (dashed lines) indicate that some residues lose more intensity than others. A number of residues display normalized intensity values that are higher (blue) or lower (red) than 1 standard deviation from average. (**F**) Space-filling model of MSI1 RRM1 (Nagata et al. 1999; Miyanoiri et al. 2003). Residues with intensities below 1 sd from the average are red. Residues with intensities higher than 1 sd from the average are blue.

Figure 4 supplement 1: Mutational analysis supports molecular dynamics simulation and docked model predictions (**A**) MSI1 RRM1 overlays from two NMR models demonstrate the highly dynamic nature of loop 3. Arginine 53 (model 1) and arginine 61 (model 3) are predicted to interact with the caboxylate of oleic acid in the respective models. (**B**) Space-filling model of MSI1 RRM1 with mutated residues colored. Orange residues indicate mutations with modest (<2 fold) or no reduction in inhibition by oleic acid. Red residues displayed a larger (>2 fold) reduction in inhibition by oleic acid. (**C**) Table of mutant RNA-binding and inhibition data. Data are the average of three independent fluorescence polarization experiments. All proteins were purified and tested during the same time period and using the same reagents, enabling comparison of wild type and mutant variants.

Figure 6 supplement 1: Dose response for oleic acid treatment in cell culture. HEK293T (dashed) and CG-4 (solid) cell proliferation as a function of increasing oleic acid (red = 50 μM, grey = 5 μM black = 0 μM). The data is the average and standard deviation of at least three biological replicates.

Figure 6 supplement 2: **(A)** MSI1 binds each of 7 SCD1 3' UTR fragments containing the MSI1 consensus sequence (G/A)U_{1-3}AGU with variable affinity. FP and F-EMSA binding experiments are reported as the average and standard deviation of three independent experiments. **(B)** The SCD1 antibody is specific for full-length SCD1 and the associated proteolysis products. Two independent shRNA constructs reduced full-length SCD1 and associated proteolysis products compared to non-transfected or control shRNA transfected HEK293T cells. (**C**) qRT-PCR of SCD1 mRNA. The data are the mean and SD of the fold-change in SCD1 mRNA from 5 independent experiments. Each experiment comprised 3 technical replicates normalized to tubulin or GTF2i.

Figure 6 supplement 3: Lipidomics analysis of undifferentiated and differentiated CG4 oligodendrocyte progenitor cells (**A**) Scatter plot of lipidomics data for differentiated vs undifferentiated CG4 cells. Data are reported as nMoles per million cells. Red data points indicate lipids that are significantly different after differentiation (FDR = 5%). (**B**) Volcano plot of lipidomics data. Dashed lines denote fold-changes of ±1.5 and ±3.

Figure 6 source data 1: Lipidomics data files.

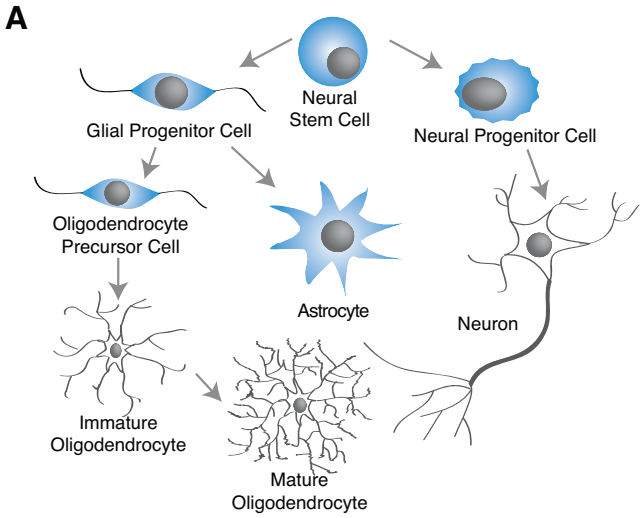
A
Neural Stem Cell
Glial Progenitor Cell
Neural Progenitor Cell
Oligodendrocyte Precursor Cell
Astrocyte
Neuron
Immature Oligodendrocyte
Mature Oligodendrocyte


B
Musashi-1
RRM1
RRM2
No MSI1
1.4 nM
2000 nM

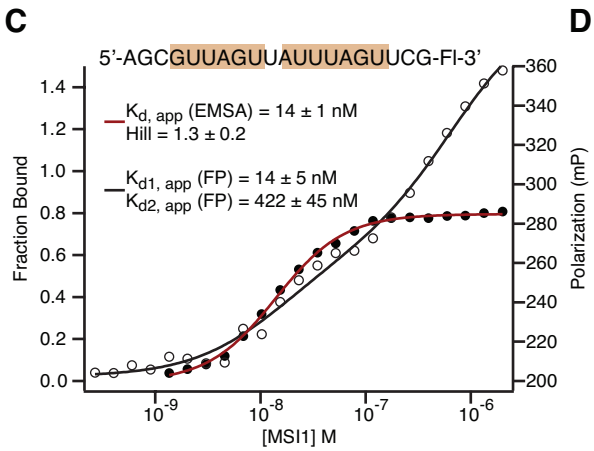
C
5'-AGCGUUAGUUAUUUAGUUCG-Fl-3'
$K_{d, app}$ (EMSA) = 14 ± 1 nM
Hill = 1.3 ± 0.2
$K_{d1, app}$ (FP) = 14 ± 5 nM
$K_{d2, app}$ (FP) = 422 ± 45 nM
Fraction Bound
Polarization (mP)
[MSI1] M

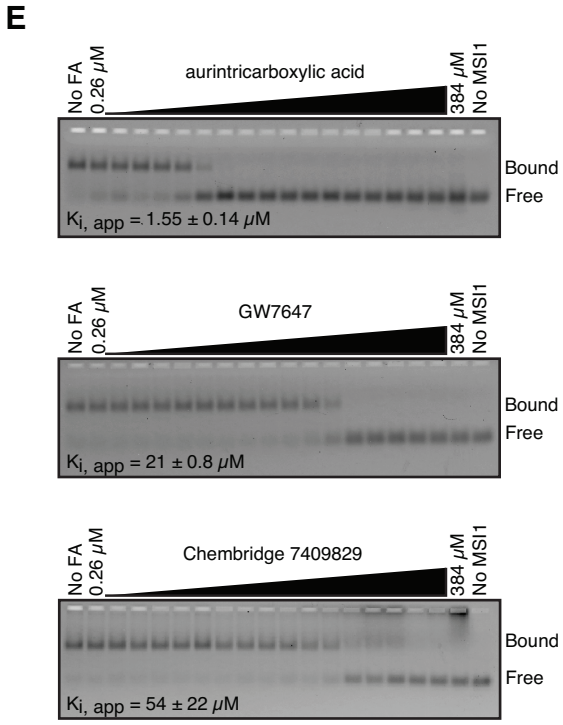
E
aurintricarboxylic acid
No FA
0.26 μM
384 μM
No MSI1
Bound
Free
$K_{i, app}$ = 1.55 ± 0.14 μM
GW7647
$K_{i, app}$ = 21 ± 0.8 μM
Chembridge 7409829
$K_{i, app}$ = 54 ± 22 μM

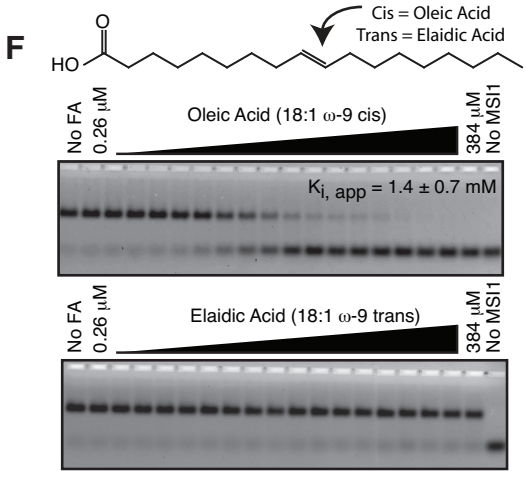
F
Cis = Oleic Acid
Trans = Elaidic Acid
HO
O
Oleic Acid (18:1 ω-9 cis)
No FA
0.26 μM
384 μM
No MSI1
$K_{i, app}$ = 1.4 ± 0.7 mM
Elaidic Acid (18:1 ω-9 trans)

Clingman Figure 2

A

Compound Name	CID	Screen Score	FP $K_{i,\ app}$ (μM)	F-EMSA $K_{i,\ app}$ (μM)
Chembridge 7409829	28425	0.045	15 ± 2.8	54 ± 22
Aurintricarboxylic Acid (ATA)	2259	0.053	0.23 ± 0.03	1.5 ± 0.14
GW7647	3397731	-0.028	6.5 ± 0.4	21 ± 0.8
Oleic Acid	445639	-0.005	1.2 ± 0.4	1.4 ± 0.7

B

Compound name	Structure	Code	FP $K_{i,\ app}$ (μM)	F-EMSA $K_{i,\ app}$ (μM)
Oleic acid	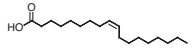	18:1 ω-9	1.2 ± 0.4	1.4 ± 0.7
Eicosenoic acid	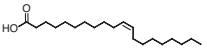	20:1 ω-9	1.2 ± 0.4	1.7 ± 0.6
Erucic acid	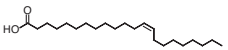	22:1 ω-9	0.64 ± 0.2	0.82 ± 0.03
Nervonic acid	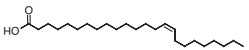	24:1 ω-9	47 ± 30	23 ± 8
Palmitoleic acid	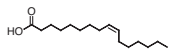	16:1 ω-7	5.3 ± 0.5	13 ± 0.9
Linoleic acid	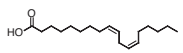	18:2 ω-6, 9	2.2 ± 0.2	1.2 ± 0.03
Arachidonic acid	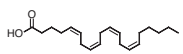	20:4 ω-6, 9, 12, 15	3.0 ± 0.2	1.1 ± 0.3
Oleoyl-CoA	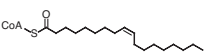	(18:1 ω-9)	8.1 ± 0.3	4.0 ± 0.2
Erucyl-CoA	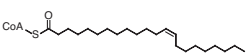	(18:1 ω-9)	4.1 ± 0.9	0.62 ± 0.2
Ricinoleic acid	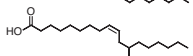	(18:1 ω-9)	No inh.	18 ± 9
Oleamide	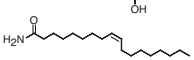	(18:1 ω-9)	No inh.	No inh.
Ethyl oleate	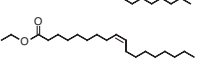	(18:1 ω-9)	No inh.	No inh.
4-Methylumbelliferyl oleate	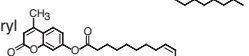	(18:1 ω-9)	No inh.	No inh.
Elaidic acid	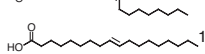	18:1(trans)	No inh.	No inh.
Stearic acid	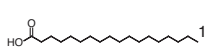	18:0	No inh.	No inh.
Palmitic acid	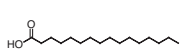	16:0	No inh.	No inh.
Myristic acid	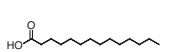	14:0	No inh.	No inh.

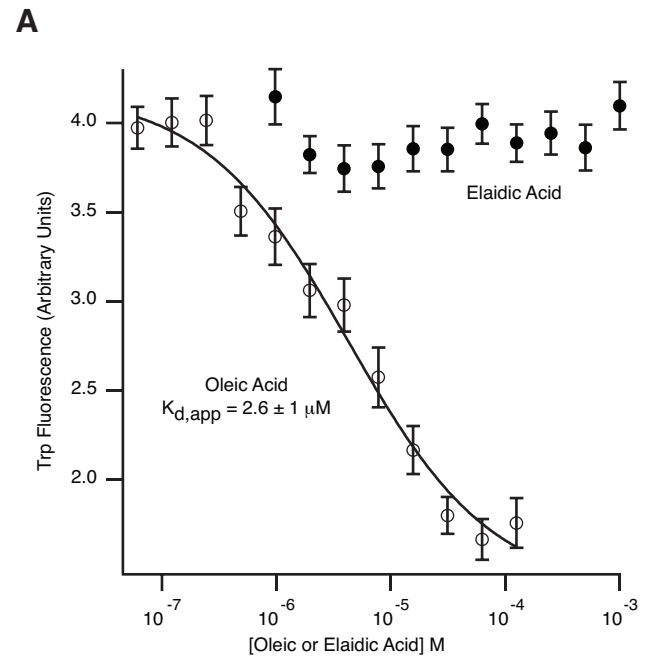
A
Trp Fluorescence (Arbitrary Units)
4.0
3.5
3.0
2.5
2.0
Elaidic Acid
Oleic Acid
$K_{d,app}$ = 2.6 ± 1 μM
10^{-7}
10^{-6}
10^{-5}
10^{-4}
10^{-3}
[Oleic or Elaidic Acid] M

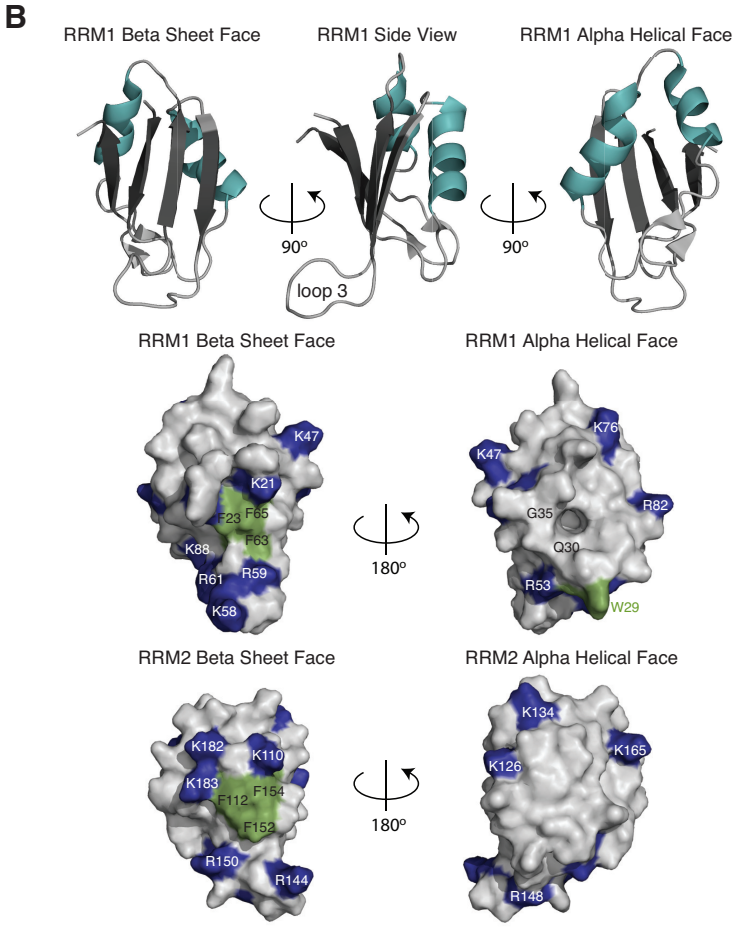
B
RRM1 Beta Sheet Face
RRM1 Side View
RRM1 Alpha Helical Face
90°
90°
loop 3
RRM1 Beta Sheet Face
RRM1 Alpha Helical Face
K47
K21
F23
F65
F63
K88
R59
R61
K58
180°
K47
K76
G35
R82
Q30
R53
W29
RRM2 Beta Sheet Face
RRM2 Alpha Helical Face
K182
K110
K183
F112
F154
F152
R150
R144
180°
K134
K165
K126
R148

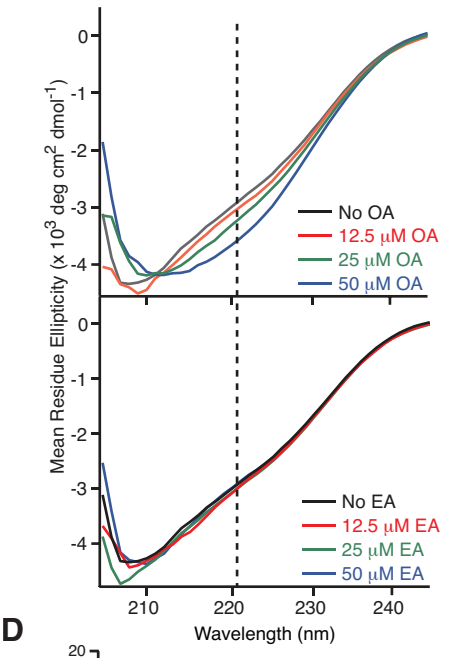
C
Mean Residue Ellipticity (x 10^3 deg cm^2 $dmol^{-1}$)
No OA
12.5 μM OA
25 μM OA
50 μM OA
No EA
12.5 μM EA
25 μM EA
50 μM EA
210
220
230
240
Wavelength (nm)

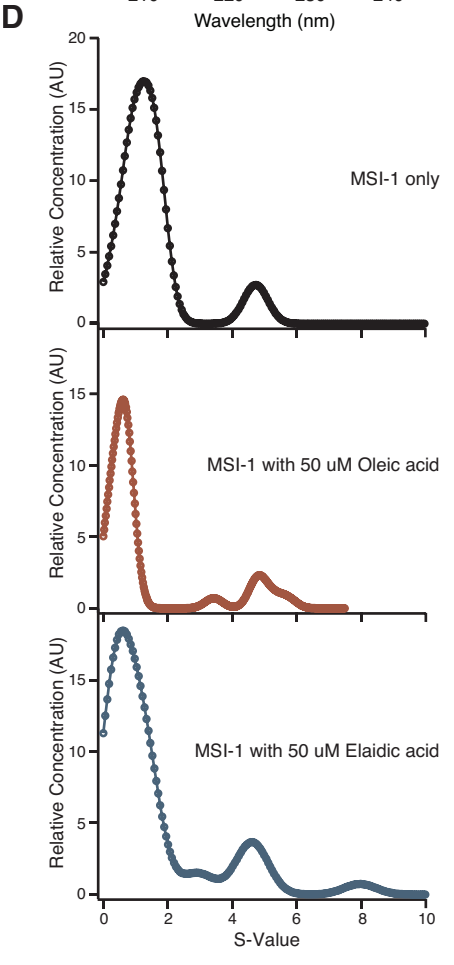
D
Relative Concentration (AU)
MSI-1 only
MSI-1 with 50 uM Oleic acid
MSI-1 with 50 uM Elaidic acid
0
2
4
6
8
10
S-Value

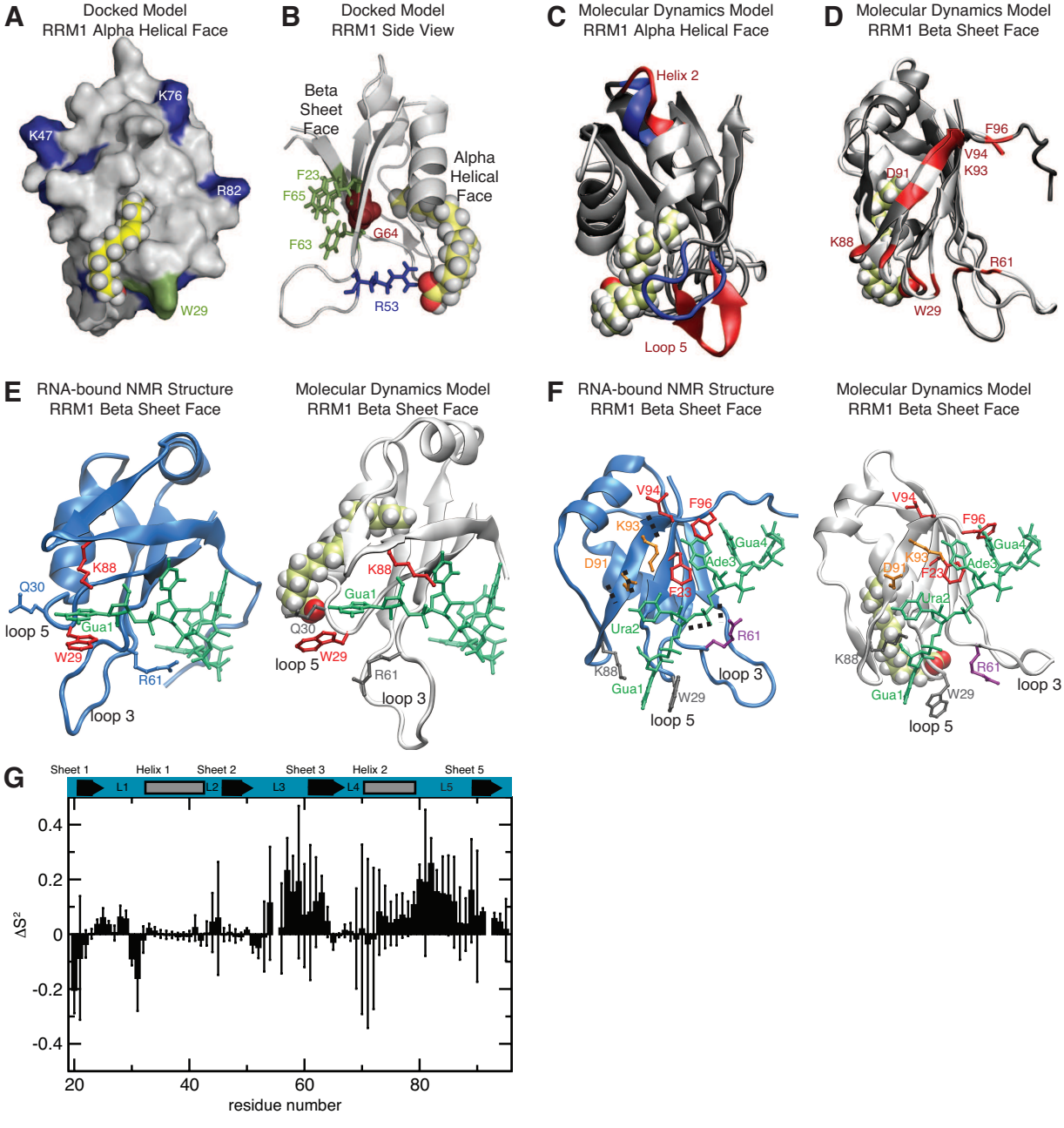
A
Docked Model
RRM1 Alpha Helical Face
K76
K47
R82
W29
B
Docked Model
RRM1 Side View
Beta Sheet Face
Alpha Helical Face
F23
F65
F63
G64
R53
C
Molecular Dynamics Model
RRM1 Alpha Helical Face
Helix 2
Loop 5
D
Molecular Dynamics Model
RRM1 Beta Sheet Face
F96
V94
K93
D91
K88
R61
W29
E
RNA-bound NMR Structure
RRM1 Beta Sheet Face
K88
Q30
loop 5
Gua1
W29
R61
loop 3
Molecular Dynamics Model
RRM1 Beta Sheet Face
K88
Gua1
Q30
loop 5
W29
R61
loop 3
F
RNA-bound NMR Structure
RRM1 Beta Sheet Face
V94
F96
K93
Gua4
D91
Ade3
F23
Ura2
R61
K88
Gua1
W29
loop 3
loop 5
Molecular Dynamics Model
RRM1 Beta Sheet Face
V94
F96
Gua4
K93
D91
F23
Ade3
Ura2
K88
R61
loop 3
Gua1
W29
loop 5
G
Sheet 1
Helix 1
Sheet 2
Sheet 3
Helix 2
Sheet 5
L1
L2
L3
L4
L5
0.4
0.2
0
-0.2
-0.4
ΔS²
20
40
60
80
residue number

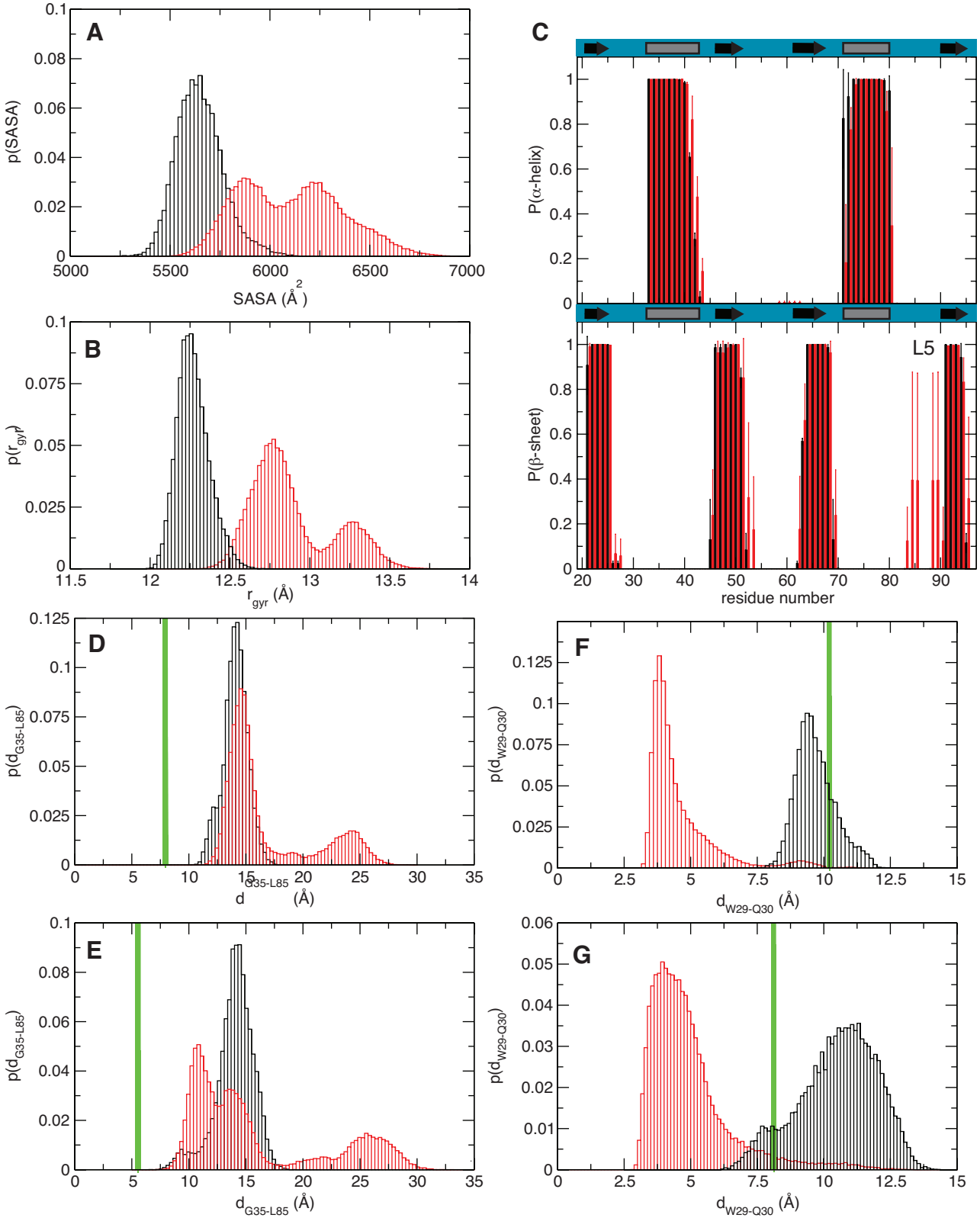
A
p(SASA)
SASA (Å^2)
B
p(r_{gyr})
r_{gyr} (Å)
C
P(α-helix)
P(β-sheet)
L5
residue number
D
p($d_{G35-L85}$)
$d_{G35-L85}$ (Å)
E
p($d_{G35-L85}$)
$d_{G35-L85}$ (Å)
F
p($d_{W29-Q30}$)
$d_{W29-Q30}$ (Å)
G
p($d_{W29-Q30}$)
$d_{W29-Q30}$ (Å)

Clingman Figure 6

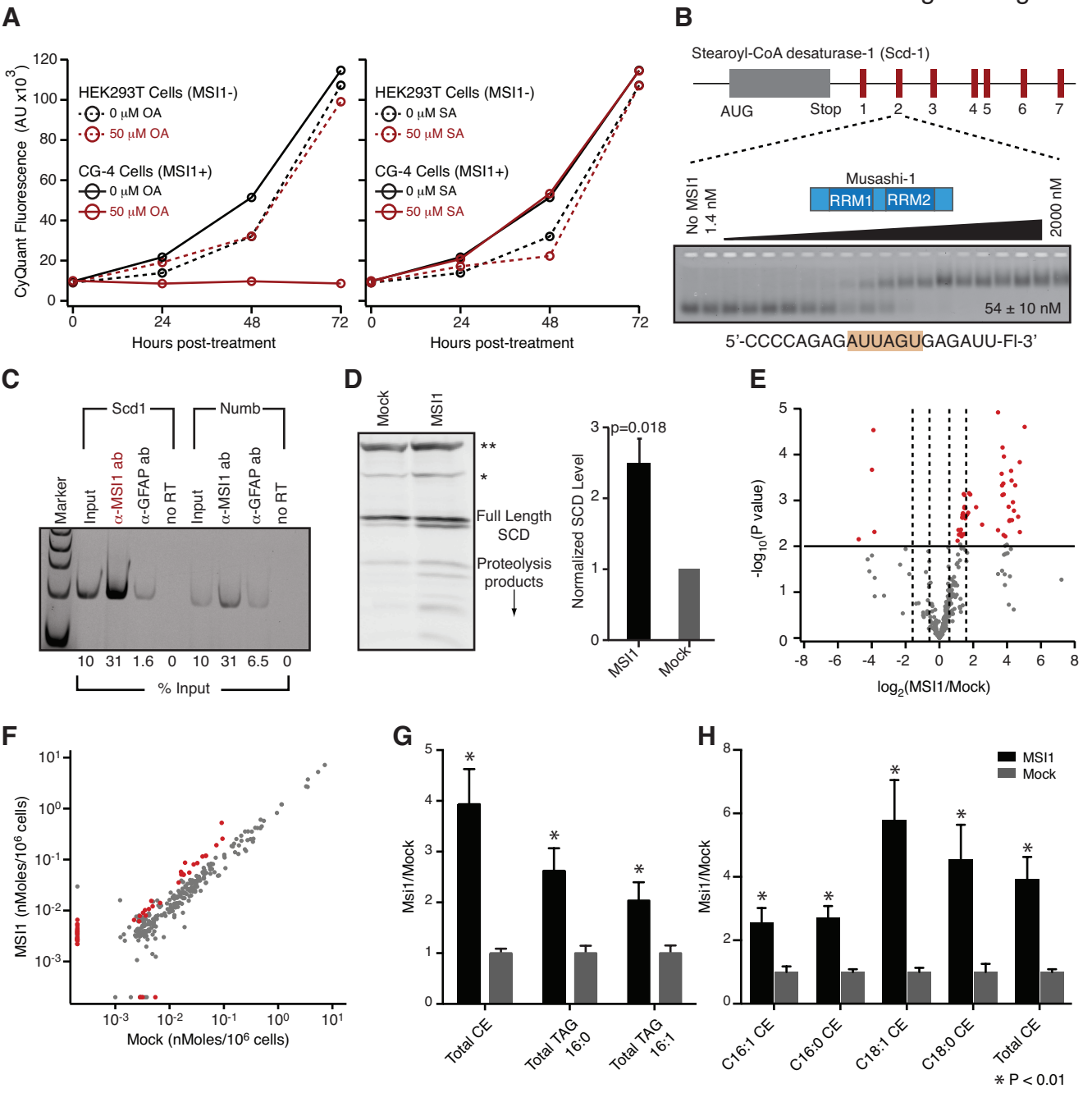

Clingman Figure 7